A Laser Setup for Two-Photon Rydberg Excitation of Potassium

Sarah Hirthe

Munich 2018

Ein Laseraufbau zur Zweiphotonen Rydberganregung von Kalium

Masterarbeit an der Fakultät für Physik
Ludwig-Maximilians-Universität München
Max-Planck-Institut für Quantenoptik

vorgelegt von

Sarah Hirthe

München, den 25. Oktober 2018

Abstract

In this thesis, a laser system for two-photon Rydberg excitation of ^{39}K is planned, constructed and characterized. The Rydberg states are addressed with a blue 405 nm laser for the 4S to 5P transition and an infrared 980 nm laser for the 5P to nS transition. The setup consists of home-built components, including external cavity diode lasers and tapered amplifiers. In order to achieve several hundreds of mW of blue light, an enhancement cavity for frequency doubling is constructed. The lasers are frequency stabilized to reference cavities, leading to linewidths below 50 kHz. The setup is optimized for a high ratio of Rabi cycles per coherence time for both single-site addressed as well as collective Rydberg excitation.

Contents

CHAPTER 1

Introduction

The field of cold atoms allows to study the behavior of dilute gases near zero temperature, which lead to the first experimental observations of Bose-Einstein condensates [1, 2] and Fermi degeneracy in trapped atomic gases [3]. Since then cold atoms have advanced to a powerful tool to study quantum many-body physics [4] and tackle fundamental problems like out-of-equilibrium dynamics and thermalization [5] in closed quantum systems. The possibility to model specific Hamiltonians in a cold atom system enables quantum simulation, where phenomena of condensed matter systems are reproduced and studied in a controlled environment [6, 7]. The most prominent setting for quantum simulation are cold atoms trapped in periodic potentials caused by standing waves of interfering laser light, so-called optical lattices [8]. On-site interaction and tunneling have been employed in optical lattices to study phenomena of the Bose-Hubbard Hamiltonian, such as phase transitions [9]. Later also the Fermi-Hubbard model has been realized using cold atoms [10, 11]. The detection using quantum gas microscopes for bosons [12, 13], and more recently also for fermions [14–17], has widened the possibilities of these setups immensely, allowing the extraction of local information through single-site resolution.

To extend the toolbox of quantum simulation, on-site interaction can be extended to long-range interactions. For long-range interacting systems there are several proposals to observe phenomena like novel quantum phases [18–20] and probe extended Hubbard models [21, 22]. One way to implement long-range interactions is by exciting neutral atoms to high lying states, so-called Rydberg states. Other platforms include magnetic atoms [23] and polar ground state molecules [24]. Rydberg atoms show strong interactions across several lattice sites with the advantage that they are tunable from attractive to repulsive, can be engineered to be isotropic or anisotropic and can be switched on and off using laser pulses. They have thus been proposed for various tasks regarding quantum simulation [25], but they are also a promising platform for quantum information and computation [26]. Recent progress using Rydberg atoms include the observation of crystallization [27], high fidelity entanglement of qubits [28], excitation to very large bound states [29] and Rydberg dressing, adding a small fraction of the Rydberg properties to the ground state atoms [30].

Closely related to the interest in long-range interacting cold atom systems is the increasing prominence of optical tweezers, which are microtraps of single atoms [31]. As compared to lattices, they allow for more flexible geometries [32] and faster cycle times, where near-deterministic loading [33] as well as reassembling [34] have been demonstrated. The project of this thesis is part of a cold atoms experiment of potassium, which uses Rydberg atoms to study quantum many-body physics with

long-range interactions. Besides the possibility for an optical lattice, the experimental setup is designed for optical tweezers and optimized for fast cycle times. Single-site resolution of the trapped atoms will be achieved by a high-resolution objective placed inside the vacuum chamber. Potassium offers the availability of both bosons and fermions and a favorable level structure for deterministic tweezer loading. The Rydberg states are accessible via two-photon as well as one-photon excitation. Setups for both excitation schemes are being build, which together will allow for simultaneous excitation of different Rydberg states and give maximum flexibility in application. This thesis is concerned with an experimental setup for two-photon Rydberg excitation of potassium, that is exciting potassium atoms to Rydberg states via an intermediate state. The design takes into account to improve the limiting parameters, which are blue laser power and laser linewidth. The setup includes home-built external cavity diode lasers and their amplification and frequency stabilization. A special focus lies on the build-up of a cavity for second-harmonic generation.

Outline

Chapter 2 introduces the relevant theoretical knowledge about Rydberg atoms and their excitation in potassium. This is then applied to the parameters given for this project to calculate the optimal design for the setup. The chapter is meant to inform about the underlying ideas and possibilities of the setup. In particular it discusses the relevant properties of potassium regarding Rydberg excitation and why certain powers, stabilities and detunings are aimed for in the setup. Chapter 3 explains the principle of second-harmonic generation in a doubling cavity. First frequency doubling, then the enhancement in a cavity is explained and the calculations done for this project are shown. In contrast to the previous chapter, this chapter is concerned with theoretical aspects relevant merely for the functioning of the setup and not for the purpose behind. Chapter 4 then presents the experimental setup. It shows the design of the different components and their characterization. It consists of two sections, namely a setup for near-infrared 980 nm light and a setup for blue 405 nm light, where the two setups correspond to the two transitions in the Rydberg excitation. The blue setup is the one which contains the doubling cavity design and characterization. Finally Chapter 5 contains a conclusion of achievements and possible improvements and an outlook of what is soon to come for the setup and its implementation into the experiment.

CHAPTER 2

Rydberg states of potassium

The chapter introduces the underlying ideas and concepts for this thesis. At first, we will discuss Rydberg atoms, their properties and the ways to excite them, especially two-photon excitation. Next, the level structure of ^{39}K will be presented. Based on that, the choice for the excitation scheme can be justified. Finally, the theoretical considerations are employed to find the optimal parameters for the setup design.

2.1 Rydberg atoms

When an outer electron of an atom is excited to a very high principal quantum number, the atom is called a Rydberg atom. Rydberg states typically have principal quantum numbers of $n \geq 20$. In principal the quantum number n can go arbitrarily high, though practically at some point close to the ionization energy there is a for practical considerations unresolved continuum of states. This limits the typical quantum numbers to $n \leq 200$ [35]. Due to their high principal quantum number, Rydberg atoms have quite exaggerated properties, that scale with the quantum number n. In the following there is a short summary of these properties. A more detailed description of Rydberg atoms can be found in [36].

Properties

An atom with only one electron in a highly excited state exhibits behavior comparable to that of a hydrogen atom. This is due to the electron charge distribution being much further away from the nucleus than the other electrons, such that those effectively shield most of the positive charge of the nucleus. Hydrogen has an electrostatic potential of

$$V(r) = -\frac{e^2}{4\pi\epsilon_0 r},$$

and corresponding quantized energy levels of

$$E_n = E_\infty - \frac{e^4 m_e}{8h^2\epsilon_0^2}\frac{1}{n^2} = E_\infty - \frac{\mathrm{Ry}}{n^2},$$

where E_∞ is the ionization energy and $\mathrm{Ry} \approx 13.6$ eV is the Rydberg constant. For Rydberg atoms the same behavior applies, though with a modified Rydberg constant Ry^*, which takes into account the reduced mass of the electron in the respective atom,

and with an adjusted quantum number $n^* = n - \delta_{nlj}$, where the quantum defect δ_{nlj} is an empirical value that accounts for the imperfect shielding of the nucleus. The energy levels are then given by

$$E_{nlj} = E_\infty - \frac{\mathrm{Ry}^*}{n^{*2}}.$$

Especially for relatively low-lying states with low angular momentum $l < 2$, where the electron is on average still relatively close to the nucleus and the other electrons, the quantum defect plays a considerable role [37]. The orbital radius is given by

$$\langle r \rangle = \frac{a_0}{2}(3n^{*2} - l(l+1)),$$

The separation of the outer electron from the rest of the atom leads to a peculiar property of Rydberg atoms, namely their van-der-Waals-like interaction, which can be over ten orders of magnitude higher than for ground state atoms [26]. From the high polarizability arises a strong dipole-dipole interaction between two Rydberg states. For long distances R this scales as $1/R^6$, giving an interaction of

$$V_{\mathrm{vdW}}(r) = -\frac{C_6}{r^6} \propto n^{*11},$$

with the coefficient $C_6 \propto \frac{(\mu_1\mu_2)^2}{E_{n+1}-E_n}$, where $\mu = \langle nl|er|nl+1\rangle \propto n^{*2}$ is the radial matrix element.
Another important property to consider, especially in the context of cold atom experiments, is the lifetime of a Rydberg state. Since the overlap of the radial wave function with that of the ground state becomes very small for higher states, the lifetimes increase rapidly, scaling as

$$\tau_0 \propto n^{*3}.$$

Due to the level separation of $\propto n^{-3}$, the Rydberg states at some point lie so close, that their level spacing is on the order of typical thermal radiation at room temperature. Thus a state can be transferred to a close-by state by the black-body radiation of the environment. The decay rate due to this stimulated emission is on similar timescales than the radiative lifetime of Rydberg atoms, scaling with

$$\tau_{\mathrm{bb}} \propto n^{*2}.$$

At very high Rydberg states it is the leading contribution to the overall decay rate.

$$\frac{1}{\tau} = \frac{1}{\tau_0} + \frac{1}{\tau_{\mathrm{bb}}}.$$

Figure 2.1 shows the effective lifetime and the contributions from the black-body-radiation-induced lifetime and the radiative lifetime for the $nS_{1/2}$ states. Black body decay dominates the overall lifetime for high Rydberg states. At n=50 both contributions are roughly equal. The lifetime is relevant when considering the optimal scheme

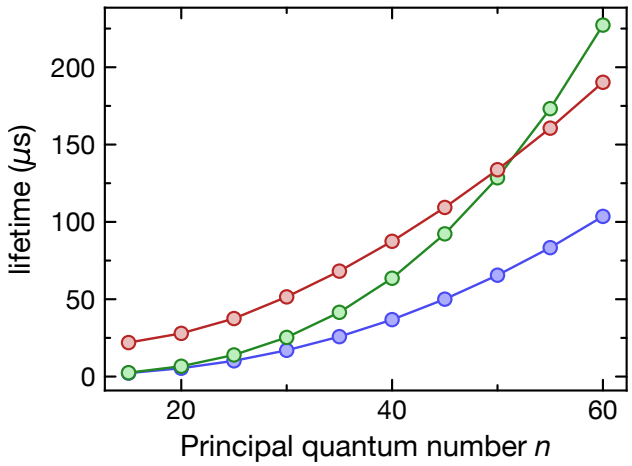

Figure 2.1 – Lifetime of the $nS_{1/2}$ Rydberg states. The scaling of the radiative lifetime τ_{rad} (green) black-body-radiation-induced lifetime τ_{BB} (red) and effective lifetime τ_{eff} (blue) for the $nS_{1/2}$ states of potassium is shown. The lifetimes are taken from [38] or calculated via the Alkali Rydberg calculator (ARC) [39].

to excite to a Rydberg state, because it marks an upper boundary for coherence times. Ideally all other contributions to the coherence time are kept lower than this limit.

Rydberg excitation

If ground state atoms are exposed to a light field resonant to a transition, they will perform Rabi oscillations [40]. In a simple model without decoherence, the probability to find the atom in the excited state goes as

$$p_2(t) = \sin^2\left(\frac{\Omega t}{2}\right), \tag{2.1}$$

with the Rabi frequency

$$\Omega = \frac{\vec{d}_{12} \cdot \vec{E}_0}{\hbar}, \tag{2.2}$$

where $\vec{d}_{12}$ is the dipole matrix element and $\vec{E}_0$ is the electric field component of the light field. When considering a laser beam with power P and waist w_0 at the location of the atoms, the Rabi frequency is thus

$$\Omega \propto \frac{\sqrt{P}}{w_0}.$$

According to equation 2.1, Rabi oscillations continue for arbitrary times, but in reality the oscillations decay over time. Relevant mechanisms for the decay are dephasing, due to laser noise and due to Doppler effect at finite temperature, and decoherence introduced through spontaneous decay of atoms [41]. For good experimental con-

trol over the atoms, it is desirable to have only a slow decay of the Rabi oscillations, respectively many Rabi cycles within the decoherence time. Estimates for the laser system in this thesis are given in the end of this chapter.
For several atoms in a lightfield resonant to the transition to a Rydberg state, interaction between Rydberg atoms play a role. Due to the interaction energy, the energy level of a Rydberg state is shifted in the presence of other Rydberg atoms. The state is shifted out of resonance with the lightfield. The blockade radius defines the distance in which the interactions are strong enough to shift the energy level out of resonance. For sufficiently big Rabi frequencies Ω it is given by

$$R_B = \sqrt[6]{\frac{C_6}{\hbar\Omega}}.$$

The blockade radius allows for several intriguing applications in experiments [27], in particular the possibility to entangle atoms and make gates between them[42], is an interesting and straight forward application for this particular setup.

Two-photon excitation

Instead of exciting a ground state atom with a light field of a single, resonant frequency, one can also drive the transition via an intermediate state. This is called two-photon excitation, since there is two different light field frequencies involved. One frequency corresponds to the transition from the ground to the intermediate state, and another to the transition from the intermediate to the excited Rydberg state. This is advantageous, since the typical transitions to Rydberg states in alkali atoms require ultraviolet (UV) light, whereas a two-photon transition is possible using only light in the visible spectrum. Coherent laser light is much easier to achieve for visible, than for UV light. However, the intermediate state has a much bigger overlap with the ground state and thus decays much faster than the Rydberg state, leading to a scattering rate that drastically decreases the coherence time. To reduce the scattering, one introduces a detuning Δ to the intermediate state, while keeping the overall transition on resonance. For large detunings, the scattering on the intermediate state scales as

$$\Gamma_{scat} \propto \frac{1}{\Delta^2}.$$

The Rabi frequency of the combined process also gets affected by the detuning and for large detunings is given by [40]

$$\Omega_{eff} = \frac{\Omega_1\Omega_2}{2\Delta},$$

where $\Omega_{1,2}$ are the one-photon Rabi frequencies. Thus the scattering decreases much faster than the Rabi frequency, allowing for a considerable reduction in scattering without completely loosing the Rabi frequency. The three-level system gets reduced to an effective two-level system. The schematics of the one- and two-photon transi-

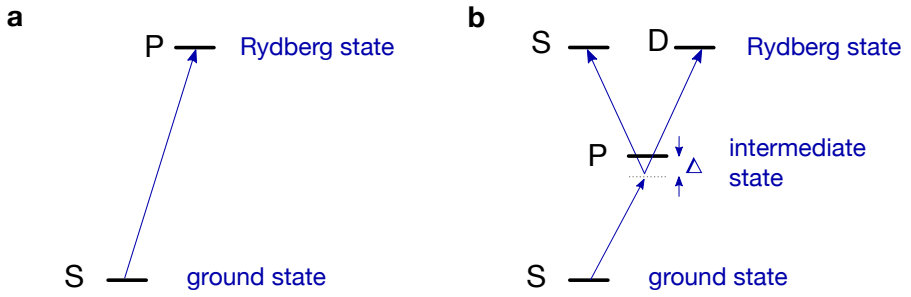

Figure 2.2 – One and two-photon excitation in alkali atoms. Figure **a** shows the schematic of a one-photon Rydberg excitation, where a single photon excites the atom from the ground state, with angular momentum $l = 0$ (S-state), to a Rydberg state with angular momentum $l = 1$ (P-state). **b** shows a schematic of the two-photon excitation, where two photons of different frequency excite the atom to the Rydberg state via an intermediate state. While the intermediate state is a P-state, the final state can either have angular momentum $l = 0$ (S-state), or $l = 2$ (D-state). The intermediate state is addressed with a detuning Δ, while the combined process is kept on resonance.

tions is shown in Figure 2.2.

Depending on the detuning, the scattering on the intermediate state can be a significant factor in the decoherence process. The detuning should be large, so it increases the coherence time, but only as long as the advantage in coherence time is bigger than the disadvantage in Rabi frequency. The choice of the optimal detuning thus depends on the limit that is set by the other sources of decoherence. The detuning should be chosen such, that the number of Rabi oscillations within the coherence time is maximized. This number can be estimated by the ratio of the effective Rabi frequency and the effective decoherence [43, ch. 5]

$$\frac{\Omega_{\text{eff}}}{2\pi\,\Gamma_{\text{eff}}} = \frac{\frac{4}{2\pi}\Omega_{\text{eff}}}{2\gamma_{\text{dep}} + 3\Gamma_{\text{dec}}}, \tag{2.3}$$

with the dephasing

$$\gamma_{\text{dep}} = \gamma_1 + \gamma_2 + \Gamma_{\text{int}}\frac{\Omega_1^2}{4\Delta^2},$$

where $\gamma_{1,2}$ is the respective laser noise and Γ_{int} the linewidth of the intermediate state and the decay

$$\Gamma_{\text{dec}} = 1/\tau_{\text{ryd}} + \Gamma_{\text{int}}\frac{\Omega_2^2}{4\Delta^2},$$

where τ_{ryd} is the lifetime of the Rydberg state. The additional term in the decay arises due to a small admixture of the intermediate state [44]. When knowing all the other parameters, the detuning can be found by optimizing this ratio. Estimations for the Rabi frequencies, coherence times and an optimized ratio, will be given by the end of this chapter.

2.2 Level structure and Rydberg excitation of ^{39}K

For the particular design of the setup the transition wavelengths for Rydberg excitation of ^{39}K have to be known. Therefore the level structure and possible transition schemes for potassium are discussed in the following.

General properties and level structure

Potassium is an alkali, hence having one electron in its outer shell. The ground state is the state $4S_{1/2}$, which has a hyperfine splitting of about 460 MHz between the two hyperfine states F=1 and F=2 [45]. This gap is large enough to address only one of the two states for excitation, but can in principle be bridged using an acousto-optical modulator (AOM), such that one setup is sufficient to drive Rydberg excitations for both hyperfine states simultaneously.

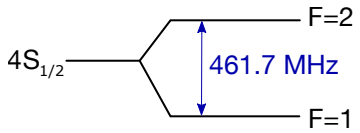

Figure 2.3 – Ground state splitting of potassium. The ground state of potassium is split into the hyperfine states F=1 and F=2 with a hyperfine splitting of $\Delta E_{\mathrm{HFS}} = 461.7\,\mathrm{MHz}$.

In Figure 2.4 the transitions from the ground state to the first few excited states are shown, as well as the transitions to the Rydberg states nS and nP using one- and two-photon transitions. The one-photon transition frequency is in the UV range. It is very challenging to build a suitable laser for these wavelengths and to achieve Rabi frequencies on the order of MHz. However, such a one-photon setup is currently being built in another master thesis [46] for the same experiment as the two-photon setup of this thesis. The two-photon transition has the advantage of transition frequencies in the visible spectrum and furthermore can be used to address isotropic S-states, as well as anisotropic D-states. The choice of the intermediate state has no effect on which Rydberg state to address, though it makes a difference in terms of dipole matrix elements, lifetimes and wavelengths. Thus the choice of an intermediate state is discussed in the following. Instead of all Rydberg states for simplicity it will now only be referred to the 50S-state as representative for all Rydberg S-states.

Inverted excitation scheme

Since the infrared D_1 and D_2 transitions in alkali atoms are most dominantly used for tasks like cooling or imaging, it is convenient to use one of these also for the intermediate state. In potassium this means using for example the $4P_{1/2}$ state as intermediate and from there going to the Rydberg state. This scheme is very commonly used for the two-photon transition, for example in [27, 41, 48] and in the following will be

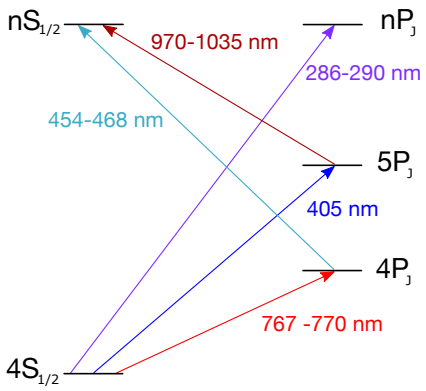

Figure 2.4 – Transitions of potassium. The transition wavelengths from the ground state to the 4P- and 5P-states are shown, as well as the two-photon transitions to the Rydberg states nS and the one-photon transition to the Rydberg states nP. The wavelengths are taken from [47] or calculated via the ARC.

called the *regular* scheme. For alkali atoms it consists of a first transition in the red or near-infrared (NIR) spectrum and a second transition typically within the range of blue.
In contrast to the regular scheme, the *inverted scheme* has the colour order inverted. This scheme is increasingly used [28, 49] to achieve higher Rabi frequencies. Instead of using the first excited state, the inverted scheme uses an intermediate state with a principal quantum number increased by one. In potassium this means using one of the 5P-states as intermediate state instead of a 4P-state. This leads to a higher transition frequency for the first transition, which then is a blue transition, and a transition in the NIR for the second transition. This scheme shows several advantages and is the one implemented in this project.

Dipole matrix elements. One advantage for the inverted scheme are the dipole matrix elements. As seen in equation 2.2, the Rabi frequency is proportional to the dipole matrix element. As seen in Figure 2.5, the regular scheme has very uneven matrix dipole elements. While the first transition has a dipole matrix element of $2.4\,a_0e$, the second transition is 400 times weaker, with a dipole matrix element of $0.006\,a_0e$. A strong imbalance in the Rabi frequencies is unfavorable, because it increases the detuning with respect to the effective Rabi frequency, which is needed to limit the scattering on the intermediate state. A further increase in Rabi frequency for the stronger transition then neither leads to a higher effective Rabi frequency, nor to a reduced scattering. The weaker transition sets a limit for the reachable effective Rabi frequency. The inverted scheme however has a more balanced relation between the two transitions. This is because the 5P-state on one hand has less overlap with the ground state, but on the other hand more overlap with the Rydberg states. The upper transition is stronger by a factor of two compared to the regular scheme.

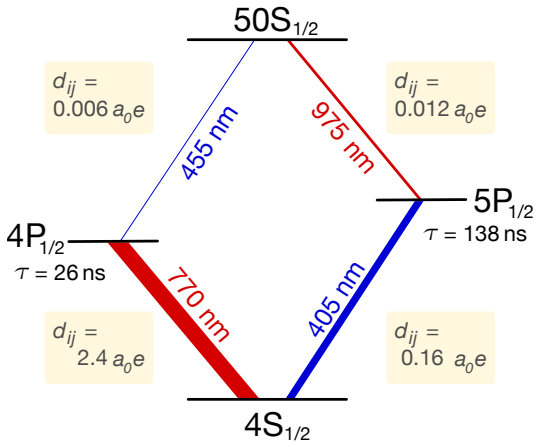

Figure 2.5 – Two-photon excitation scheme with dipole matrix elements. On the left is the regular scheme for Rydberg excitation and on the right the inverted scheme. In gray are the dipole matrix elements in each transition, calculated via the ARC.

Transition wavelengths. A closely related advantage comes with the color order of the inverted scheme. While the regular scheme needs the blue wavelength with the weaker transition, the inverted scheme has the blue transition first. The blue transition is more than 20 times stronger in case of the inverted scheme. This is relevant because blue lasers are much more limited in power than NIR lasers. For NIR there are amplifiers that can amplify a diode laser up to a few watts, as in this project, or even up to tens of watts if needed, using Raman amplifiers [50]. Such amplifiers do not exist in the blue range. Furthermore blue laser are less stable and often limited to a few mW output power for single mode operation. This is why most experimental setups that need blue laser light use either frequency doubling [27, 41] or injection locking, a configuration where a stabilized laser seeds another diode, to achieve considerable output power [28]. It is thus beneficial to have the red/NIR transition with the smaller dipole matrix element and the blue transition with the bigger matrix element. For the NIR transition much more power can be achieved and consequently the Rabi frequency can be higher, as $\Omega \propto \sqrt{P}$. The technological limitation of having much higher power in the NIR than in the blue is evened out by the different transition strengths, instead of being amplified as in the regular scheme.

Intermediate state lifetime. Another important difference between the two excitation schemes, are the lifetimes of the intermediate state. While the 4P-states have a lifetime of $\tau_{4P} \approx 26\,\text{ns}$, the 5P-state has a lifetime of $\tau_{5P} \approx 138\,\text{ns}$ [47]. This means that there is about 5 times less scattering on the 5P-state, than on the 4P-state and thus less detuning is needed. This advantage allows for longer coherence times.

2.3 Estimation for the parameters of the laser system

The aim of this section is to motivate the choices that were made for the setup. The Rabi frequencies and coherence times achievable with the inverted scheme for potassium are estimated using the equations introduced earlier in the chapter. The calculations show that the laser linewidths are a limiting factor for the Rabi cycles per coherence time and several GHz detuning is needed to keep scattering on the intermediate state low. This motivates the use of a cavity lock for the lasers of both transitions. The laser powers are an equally limiting factor, leading to the conclusion that a doubling cavity is the best choice to generate the 405 nm blue light.
The calculations are done for two different scenarios, because the potassium experiment offers two different paths for addressing the atoms with light. The first path is to address all atoms simultaneously, leading to delocalized excitations. For this case a beam waist of $w_0 \approx 50\,\mu\text{m}$ for both lasers is assumed to estimate the parameters. The second path is a special advantage of the experiment design, which is to focus the NIR light of the upper transition to a single atom. This means single-atom gates on any particular site can be realized. The reduced waist of $w_{0,\text{NIR}} = 1\,\mu\text{m}$ increases the Rabi frequency according to $\Omega \propto w_0^{-1}$ and thus leads to different parameters.
In a first step the required blue laser power is estimated. The idea is that the number of Rabi cycles per coherence time is limited by the weaker Rabi frequency according to equation 2.3. An increase in the stronger Rabi frequency requires a proportional increase in the detuning to not decrease coherence times, rendering it without any effect. Assuming that $P = 500\,\text{mW}$ are a lower limit for the reachable NIR power, it is thus relevant to know how much blue power is required to achieve comparable Rabi frequencies. The following table lists the Rabi frequencies for both scenarios, single site and all atom addressing and shows the blue power required in order to reach the same Rabi frequency. The waist of the blue laser can not be focused and is in both cases assumed with $w_0 = 40\,\mu\text{m}$.

scenario	P_{NIR} (W)	$\Omega_{\text{NIR}}/2\pi$ (MHz)		P_{blue} (W)
single atom	0.5	2400	$\rightarrow$	2
all atoms	0.5	50	$\rightarrow$	0.01

Table 2.1 – Required blue power for balanced Rabi frequencies. The expected Rabi frequencies for the NIR transition are calculated together with the required blue power to reach the same Rabi frequency for the blue transition.

The table shows that for the focused case the Rabi frequency of the NIR transition is very high. Blue light of 2 W power is not feasible in this project. This means that the blue transition is limiting the effective Rabi frequency for single atom gates. In this project a doubling cavity is build for the blue light in order to increase the reachable blue Rabi frequency. In the other scenario, where all atoms are addressed, only a few mW of blue are needed. Assuming that the doubling cavity has several 100 mW of output, this means that for that case the NIR power is the limiting factor.

Having an idea of the single-photon Rabi frequencies it is now relevant to know where the optimal detuning will be in order to design the setup. It might be possible to lock the blue laser to the 4S to 5P transition frequency and introduce the detuning using an acousto-optic modulator (AOM), but it might also be that a cavity lock is needed to go to higher detunings. In this case it turns out that a cavity lock is needed both because of the high detuning needed and because of a low laser linewidth being desirable. The optimal detuning can be estimated by calculating the ratio of Rabi frequency and decoherence of equation 2.3. For this setup a NIR laser power of 500 mW to 1 W is feasible. For the blue laser the cases of 50 mW to 200 mW are compared to observe the effect on the detuning. For the linewidth of the laser light the cases of 100 kHz and 10 kHz linewidth are compared to show the crucial effect the linewidth has on the decoherence.
In Figure 2.6 the ratio of effective Rabi frequency and effective decoherence is plotted against the detuning for both addressing scenarios and for different powers and laser linewidths. As discussed before, the ratio of effective Rabi frequency and decoherence gives the approximate number of Rabi cycles within the $1/e$-coherence time. The optimal detuning lies at the maximum of the curves. The $\Omega_{\text{eff}}/\Gamma_{\text{eff}}$-ratio in each case is plotted for a laser linewidth of 100 kHz and a laser linewidth of 10 kHz. For the case of addressing a single atom, a power of the NIR laser of 100 mW is assumed. More power only leads to a higher detuning necessary, but not to a significant improvement of the $\Omega_{\text{eff}}/\Gamma_{\text{eff}}$ ratio. The ratio is plotted for the cases of 50 mW of blue light and for 200 mW of blue light. For the unfocused case 100 mW of blue light are assumed, with the same argument of more blue power not improving the ratio. The ratio is then plotted for 500 mW and 1.5 W of NIR light.
In both cases the 10 kHz linewidth leads to a two times better ratio than the 100 kHz linewidth, showing that the laser linewidth is a limiting factor. A further linewidth reduction is not considered in this plot, since it does not drastically improve the ratio. A further reduction by a factor of ten, to a 1 kHz linewidth, improves the ratio by about 20%. In the single atom case the blue light is clearly limiting, where a four times higher power gives a two times better ratio, directly corresponding to the proportionality in the single atom Rabi frequency. The higher blue power does not influence the optimal detuning, showing that the NIR transition is dominating the detuning needed. In the case of addressing all atoms the NIR light is the limiting factor, where an increase in power of a factor 3 increases the ratio by a factor of $\sqrt{3}$, while not increasing the optimal detuning. The blue transition is much stronger in this case, determining the overall detuning. This shows again that it is crucial to aim for the most NIR power possible, the most blue power possible and the smallest linewidth possible. The detuning for all cases lies in the range of 1 to 10 GHz, which can be accomplished locking the blue laser to a cavity. A small deviation from the optimal case does not have much effect.
Limitations of this calculation are the missing consideration of laser phase noise above the lock bandwidth, a known limitation of coherence times in Rydberg excitation [41]. A possibility to reduce the high-frequency phase noise is the use of a filter cavity [28], which is however not done in this project. Also the dephasing due to Doppler shifts in finite temperature are not considered here. They are however reported to be negli-

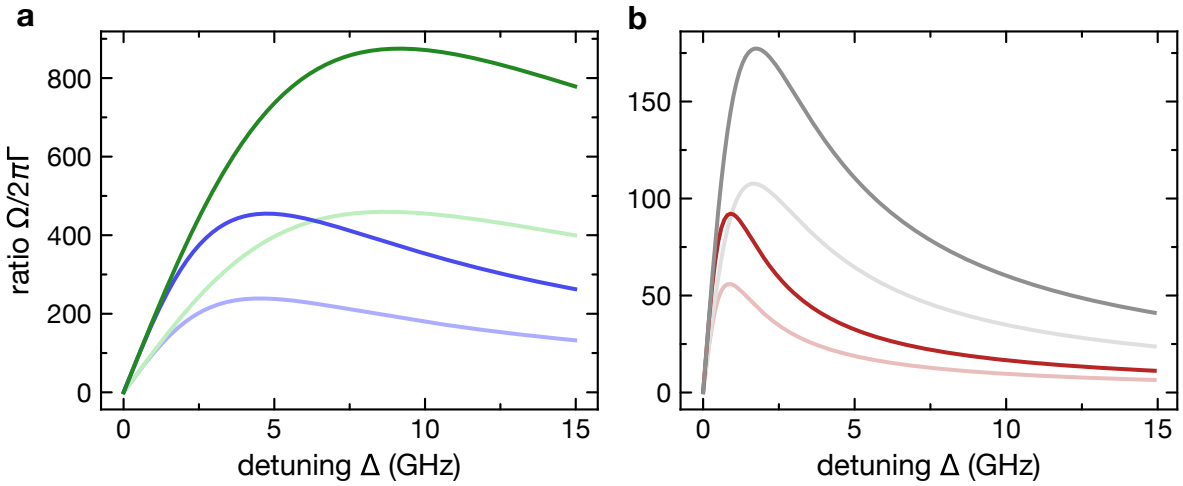

Figure 2.6 – Optimal detuning for the two-photon excitation. Both plots show the ratio of effective Rabi frequency and effective decoherence against detuning. The maximum of the curve marks the optimal detuning. In figure **a** is the case for single atom addressing with a NIR laser of 100 mW power and 1 µm waist, and a 40 µm waist for the blue light. The light blue and light green lines show the case of 50 mW blue light and the darker lines are calculated for 200 mW of blue. The blue lines show the curve for a laser linewidth of 100 kHz, whereas the green lines are plotted for 10 kHz linewidth. In **b** is the case of addressing all atoms. The blue laser is assumed to give 100 mW of blue light with a waist of 40 µm, and a NIR waist of 50 µm. Light red and gray correspond to 500 mW of red light, dark red and gray to 1.5 W. The red lines correspond to 100 kHz of linewidth and the gray ones to 10 kHz. In all cases the decoherences is calculated including the black-body-radiation-induced decay.

gible in the µK regime with several MHz of effective Rabi frequency [41].
The conclusions from these calculations for the setup are, that NIR laser will be be amplified using a tapered amplifier which can reach an output power of 2 W. The blue light will be achieved via frequency doubling an amplified NIR laser in an enhancement cavity. This way 100 mW to 400 mW of blue light can be achieved. Both lasers will be frequency stabilized to cavities, allowing for kHz-regime linewidths and arbitrarily high detunings.

CHAPTER 3

Cavity-enhanced second-harmonic generation

This chapter presents the theoretical background and calculations for frequency doubling. Frequency doubling is employed in this project to generate coherent 405 nm light out of a 810 nm laser beam, in order to address the $4S_{1/2} \rightarrow 5P_{1/2}$ transition in ^{39}K. The first section introduces the relevant aspects of single-pass theory for frequency doubling in a nonlinear crystal and discusses single-pass optimization. Section 3.2 contains calculations for the geometry of the doubling cavity as well as for the mirror coatings inside the cavity.

3.1 Theory of second-harmonic generation

3.1.1 Nonlinear crystals

A nonlinear material responds to an applied optical field in a nonlinear way. Generally the polarization of a material in presence of a field with strength $\tilde{E}(t)$ can be described as

$$\tilde{P}(t) = \epsilon_0[\chi^{(1)}\tilde{E}(t) + \chi^{(2)}\tilde{E}^2(t) + \chi^{(3)}\tilde{E}^3(t) + ...],.$$

where ϵ_0 is the permittivity of free space and $\chi^{(1)}$ is the linear optical susceptibility, $\chi^{(2)}$ the second order, and $\chi^{(3)}$ the third order nonlinear susceptibility, and so forth. For nonzero second-order susceptibility $\chi^{(2)}$, the nonlinear optical interactions can lead to the generation of radiation at the second harmonic frequency as follows. When a laser beam with the electric field strength of

$$\tilde{E}(t) = Ee^{-i\omega t} + \text{c.c.} \tag{3.1}$$

interacts with the material, the nonlinear polarization is given by

$$\tilde{P}^{(2)}(t) = \epsilon_0\chi^{(2)}\tilde{E}^2(t) = 2\epsilon_0\chi^{(2)}EE^* + (\epsilon_0\chi^{(2)}E^2e^{-i2\omega t} + \text{c.c.}). \tag{3.2}$$

The first term corresponds to a DC-offset of the polarization, whereas the second describes an oscillation. This oscillation of the dipole moment leads to the generation of radiation at 2ω, the second harmonic frequency. The process can be pictured as three-wave mixing with the destruction of two photons of frequency ω and a simultaneous creation of one photon at frequency 2ω.

3.1.2 Phase matching

For efficient second-harmonic generation it is crucial that the generated radiation at the second harmonic does not interfere destructively. If waves travel through the material with different phases, they will cancel each other, whereas phase matching of the waves guarantees constructive summation of the waves. This condition can be pictured in the following way [51]. A photon of frequency 2ω being created at a point $z = 0$ picks up a phase

$$\Phi_{2\omega}(z) = 2\pi n_{2\omega} \frac{z}{\lambda_{2\omega}}$$

while traveling through the material, where $n_{2\omega}$ is the frequency dependent refractive index of the material and $\lambda_{2\omega}$ is the wavelength of the second harmonic. On the other hand, a photon created at a point z_0, has a phase depending on the fundamental wave. If the fundamental has picked up a phase of

$$\Phi_{\omega}(z_0) = 2\pi n_{\omega} \frac{z_0}{\lambda_{\omega}},$$

then the second harmonic is created with a phase of $2\Phi_{\omega}(z_0)$. This follows from taking the z dependence into account in equation 3.1 and 3.2. Thus, the second harmonic interferes constructively at z_0 if the phase matching condition

$$\Phi_{2\omega}(z_0) = 2\Phi_{\omega}(z_0)$$

is fullfilled. This is the case for

$$n_{2\omega} = n_{\omega}.$$

In this thesis phase matching is achieved via so-called *critical phase matching*, where birefringence of a crystal is used to adjust the refractive indices. Birefringence refers to the polarization dependence of the refractive index. The so-called *extraordinary* axis has refractive index n_e for all light rays polarized parallel to this axis, whereas all light rays perpendicular to this axis experience *ordinary* refraction n_o. In this case there is one extraordinary axis and two ordinary axes.
Type I critical phase matching (o-o-e), which is employed in this project, means that the fundamental wave is polarized along an ordinary axis. The second harmonic is created with perpendicular polarization to the fundamental. The polarization axis of the second harmonic is a linear combination of an ordinary axis with the extraordinary axis. By adjusting the proportion of extraordinary axis, the refractive index for the second harmonic can be tuned. This adjustment is done by cutting the crystal in a specific angle and is not tunable afterwards. Figure 3.1 illustrates the relation of the different axes. Further elaboration on the topic of nonlinearity and phase matching can be found in [52].

3.1.3 Barium borate (BBO) crystal

In this project, a beta-barium borate (BBO) crystal is used for second-harmonic generation. BBO is largely applied for generation of second harmonics in the visible and

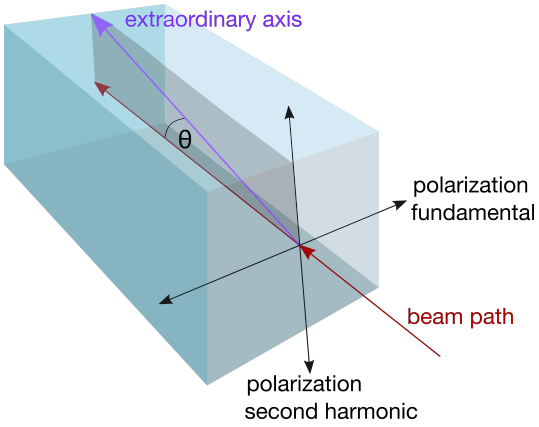

Figure 3.1 – Birefringent axes in type I phase matching. The crystal is shown with the beam propagating along the beam path. The second harmonic is generated with a polarization perpendicular to the fundamental. The extraordinary axis of refractive index n_e lies in the plane of beam path and second-harmonic-wave polarization. By changing the phase matching angle θ of the extraordinary axis in this plane, the refractive index for the second harmonic wave is adjusted. The fundamental wave is polarized perpendicular to that plane and never experiences the extraordinary refraction.

Quantity	Value
walk-off ρ	67.37 mrad
effective nonlinearity d_{eff}	2 pm V^{-1}
phase matching angle θ_{pm}	29°
refractive index $n_\omega = n_{2\omega}$	1.659
Brewster angle θ_{B}	58.92°

Table 3.1 – Properties of BBO. Properties of BBO for type I frequency doubling from 810 nm to 405 nm at a crystal temperature of 82°C.

UV-range due to its wide transparency range from the UV to the near infrared [53], and large effective nonlinearity $d_{\text{eff}} = \frac{1}{2}\chi^{(2)}$ [54]. It is nonhydroscopic, however its surfaces are likely to deteriorate due to atmospheric moisture [55], which is why the BBO in this project is temperature stabilized at 82°C. Furthermore, BBO suffers from a walk-off in the second harmonic, meaning that the generated wave propagates under an angle with respect to the fundamental. This angle adds up over the length of the crystal and leads to an elliptical output in the second harmonic. Additionally, due to the divergence of second harmonic and fundamental, the conversion efficiency decreases quickly [52]. From the SNLO [56], a freely available program, one gets the properties for BBO for type I frequency doubling from 810 nm to 405 nm at a temperature of 82°C, as can bee seen in table 3.1.

3.1.4 Boyd-Kleinman theory

The first step towards reaching a good conversion efficiency for frequency doubling is to optimize the conversion for a single pass of the fundamental beam through the crystal. Second-harmonic generation is a quadratic effect, meaning that the conversion depends quadratically on the intensity of the fundamental. Thus a higher intensity in the crystal results in better conversion. This means that a smaller beamwaist leads to better efficiency, because it increases intensity. However, a tighter focus leads to higher divergence and thus less efficiency far from the focus. Consequently, the task is to find the optimum trade-off waist, focusing to a high conversion efficiency in the center without decreasing it significantly outside of the focus.
In 1968, G. D. Boyd and D. A. Kleinman presented their theoretical study on the optimization of second-harmonic generation [57]. They consider a focused Gaussian beam in a nonlinear crystal with different refractive indices for the fundamental and second harmonic beam and a resulting walk-off. They derive the power of the generated second harmonic wave as given by the expression

$$P_{\mathrm{SH}} = P_{\mathrm{F}}^2 \, \frac{16\pi \, L \, d_{\mathrm{eff}}^2}{c \, \lambda_{\mathrm{F}}^3 \, n_{\mathrm{SH}} \, n_{\mathrm{F}} \, \epsilon_0} \, h(\sigma, B, \xi) = P_{\mathrm{F}}^2 \, \kappa_{\mathrm{NL}},$$

where the nonlinear coefficient κ_{NL} contains all factors different from the fundamental power. $P_{\mathrm{SH/F}}$ are the respective powers of the second harmonic and fundamental, $n_{\mathrm{SH/F}}$ the refractive indices, λ_{F} the wavelength, L the length of the crystal and $h(\sigma, B, \xi)$ the Boyd-Kleinman-factor. The Boyd-Kleinman-Factor contains all geometric dependencies of the conversion. In this formulation it is already assumed that the focus lies in the center of the crystal and the absorption for the second harmonic wave is zero. The parameters for the Boyd-Kleinman-factor are $\sigma = \frac{1}{4}\Delta k z_0$ describing the phase mismatch with $\Delta k = k_{\mathrm{SH}} - 2k_{\mathrm{F}}$ and the Rayleigh range z_0, the B-parameter $B = \frac{\rho\sqrt{l k_{\mathrm{F}}}}{2}$ describing the walk-off with the walk-off angle ρ and the last parameter $\xi = \frac{L}{2z_0}$, which describes the focal strength of the fundamental in the crystal. With these parameters $h(\sigma, B, \xi)$ is given by

$$h(\sigma, B, \xi) = \frac{1}{4\xi} \int_{-\xi}^{+\xi} \int_{-\xi}^{+\xi} d\tau d\tau' \frac{\exp\big(- i\sigma(\tau' - \tau) - \frac{B^2(\tau' - \tau)^2}{\xi}\big)}{(1 + i\tau')(1 - i\tau)}. \tag{3.3}$$

Optimization

To optimize the single-pass efficiency, one has to optimize the Boyd-Kleinman parameter in equation 3.3. There is a simple analytical expression to reproduce in good accordance the optimized parameters for the Boyd-Kleinman-factor [58], which takes into account the B and ξ parameters. However in this case the full numerical optimization is done, but also depending on the phase mismatch σ, as well as on ξ, but not on the walk-off B. The B-parameter is fixed by limiting the crystal length to 10 mm. This is set in order to limit the ellipticity of the output beam, which is not considered by the Boyd-Kleinmann parameter. Ellipticity decreases the obtained fraction of the generated second harmonic, because only the Gaussian fraction of the elliptic beam

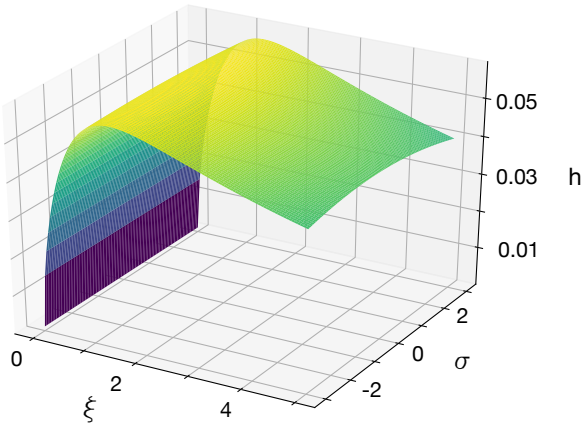

Figure 3.2 – Boyd-Kleinman optimization. Value for the Boyd-Kleinman parameter h depending on the focal strength ξ and the phase mismatch σ. While h has a strong dependence on ξ with a maximum of $h = 0.058$ for $\xi = 1.41$, there is basically no dependence on σ for small deviations from $\sigma = 0$.

is used. 10 mm has shown to be a good value to get considerable conversion with acceptable ellipticity [43, ch. 5]. Figure 3.2 shows a 2D Plot of the Boyd-Kleinman-factor. The maximally reachable value is $h = 0.058$ for a focal strength of $\xi = 1.41$. The waist for the optimized focal strength can be calculated as

$$w_{0,\mathrm{opt}} = \sqrt{\frac{\lambda_\mathrm{F}\, z_0}{n_\mathrm{F}\, \pi}} = \sqrt{\frac{\lambda_\mathrm{F}\, 2\xi}{n_\mathrm{F}\, l\, \pi}} = 23.4\,\mu\mathrm{m}.$$

For small σ the values of h stays basically constant, such that the phase mismatch in this work was set to

$$\sigma = 0 \qquad \rightarrow \qquad \Delta k = 0.$$

This corresponds to the phase matching angle as given in table 3.1. For other frequencies and other crystals the phase matching angle must not always give the optimum efficiency, since the phase matching condition, as discussed in Section 3.1.2 is derived for a collimated beam. For a strongly focused beam this does not always lead to all second harmonic waves interfering constructively.

Deviation from the optimum

In the previous section the phase mismatch and waist in the crystal have been optimized to give the highest possible single-pass conversion efficiency. In reality this optimum is problematic, because the effect of thermal lensing can appear. A focused beam of high intensity in the center of the crystal leads to heating, changing its properties. In particular the refractive index and thus the phase matching condition are dependent on temperature. Thus, if the crystal heats up inhomogeneously, the phase

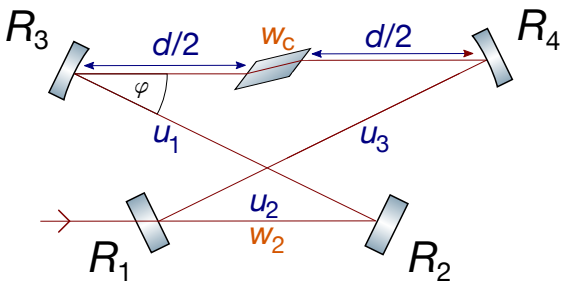

Figure 3.3 – Schematic of a bow-tie ring cavity. The cavity has two flat mirrors R_1 and R_2 as well as two curved mirrors R_3 and R_4. The crystal is in distance $d/2$ between the two curved mirror along the short arm with waist w_c. The long, collimated arm has waist w_2 and length $u = \Sigma_i u_i$. The beam enters the cavity through the partially reflective mirror R_1.

matching changes throughout the crystal, causing a severe drop in conversion efficiency.
For the intensity in a single pass, this would not be a problem. However, in this thesis a cavity is build to enhance the power of the fundamental and thus the conversion. In this doubling cavity round trip powers of 100 W can be reached. To minimize the chance of thermal lensing effects in the cavity, the focal strength in this setup is reduced by a factor of 3. The waist is thereby made bigger by a factor of $\sqrt{3}$, and the peak intensity in the cavity is three times smaller. Still the Boyd-Kleinman-Factor stays relatively close to its optimum, having a value of

$$h_{\text{red}} = 0.046.$$

The waist is then given by

$$w_{0,\text{red}} = 40.6\,\mu\text{m}.$$

This method has been employed before with good results [59].

3.2 The optical resonator

The single-pass efficiency, even for the optimized case, is not sufficient to convert a considerable fraction of the fundamental to the second harmonic. The nonlinear coefficient κ_{NL} in table 3.3, shows a conversion efficiency of less than 0.5% for a fundamental of 2 W power. A cavity to enhance the power in the crystal can increase this conversion by a factor of 50 [43, 60–62]. This work uses a bow-tie ring cavity, whose schematic is shown in Figure 3.3. The cavity consists of two curved mirrors R_3 and R_4 with curvature $R = 50\,\text{mm}$ as well as two flat mirrors R_1 and R_2. The BBO crystal is centered in between the curved mirrors with distance $d/2$ to both sides. The curvature of the mirrors causes the strong focus with waist w_c inside the crystal. The long arm, that is the path going via the flat mirrors, has length $u = \Sigma_i u_i$ and the waist w_2 is nearly constant all along the path. The beam is coupled into the cavity through the

partially reflective mirror R_1. The mirrors R_2, R_3 and R_4 are highly reflective for the fundamental, though transmissive for the second harmonic, such that the second harmonic is coupled out straight through mirror R_4 after being generated in the crystal. The BBO crystal is cut in a Brewster cut angle, which leads to a kink in the beam path due to refraction. The Brewster cut avoids reflections on the surface of the crystal. An AR coating is not an alternative as the AR coatings are reported to have a low damage threshold [63].

3.2.1 Stability

One requirement for the cavity is that the beam has to be mapped onto itself after an arbitrary amount of round trips. Cavity stability means that the beam remains inside the cavity and does not diverge. The derivation of the stability condition is not reproduced here, but can be found for example in [64]. Stability of the resonator is accordingly given for

$$0 \leq \gamma_1 \gamma_2 \leq 1, \tag{3.4}$$

where

$$\gamma_1 = \frac{-l(1-\frac{1}{n}) - d + R}{R},$$
$$\gamma_2 = 1 - \frac{u}{R},$$

where R is the curvature of the curved mirrors. The q parameter of the Gaussian beam has to be mapped onto itself after a single round trip for the Gaussian TEM_{00} mode to propagate in the cavity. This is the self-consistency condition

$$q = q_1 = q_2.$$

Using the already set parameters of Section 3.1.4, this leads to the condition

$$\alpha^2 := \frac{n^2 \xi R^2}{l} \stackrel{!}{=} \frac{\gamma_2}{\gamma_1(1-\gamma_1\gamma_2)}, \tag{3.5}$$

This equation marks a one-dimensional curve inside the two dimensional region of stability. The stability region of equation 3.4 can be identified as the condition of any real solution of α. In order to get a maximally stable solution, the minimum of the curve in equation 3.5 has to be identified. At this point the curve is located most central in the stability region.
One also has to take into account that the Brewster cut introduces astigmatism [65]. When the Gaussian beam is projected onto the crystal surface, the waist is stretched in the tangential plane and the beam becomes elliptic. This leads to the stability regions for the sagittal and the tangential plane slightly differing from each other. For the exact values characterizing the ellipticity in the crystal, one needs to already know the full geometry of the cavity, in particular the length of the two arms and the incidence angle of the beam on the mirrors. They define in which shape the beam will be projected onto the Brewster cut. Thus the procedure in this project went as follows.

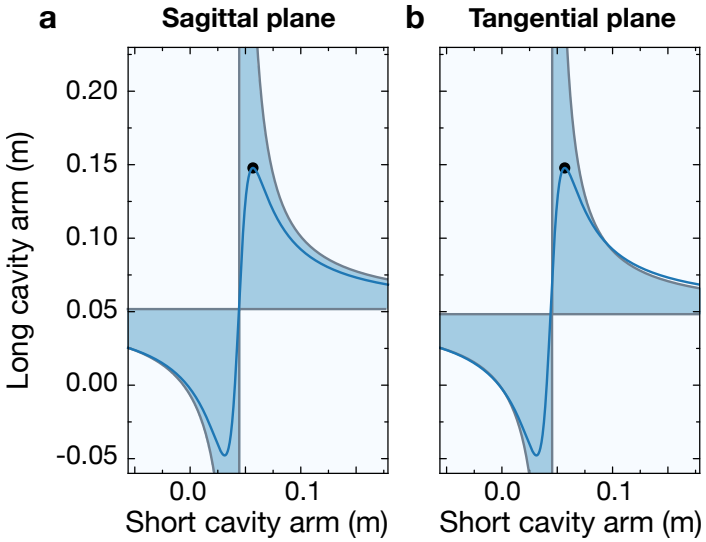

Figure 3.4 – Stability of the sagittal and tangential cavity plane. The shaded areas show the regions where the lengths of the long and short arm fulfill the stability condition. Figure **a** shows the stability condition for the sagittal plane (perpendicular to the cavity plane), **b** for the tangential plane (parallel to the cavity plane). The blue line indicates self-consistency for the calculated crystal length and focal strength. The black dot marks the chosen value for the long and short arms of the cavity.

The geometry of the cavity is chosen as the maximum of equation 3.5 neglecting the astigmatism of the cavity. Then, as discussed in the next part the angle of incidence on the mirrors is calculated. Afterwards the alteration of the stability conditions can be calculated. The stability can then be checked again taking into account the astigmatism. In Figure 3.4 the final stability regions for the tangential and the sagittal plane are shown. Additionally, the figure contains the original line defined by equation 3.5 if astigmatism is ignored. The figure shows that the maximum of this line indeed lies within the stability region for both planes. It is thus a good choice for the cavity geometry.

3.2.2 Astigmatism

The curved mirrors R_3 and R_4 are an astigmatic element in the cavity. For an incidence angle φ different from zero they cause different focal lengths for the tangential ($\widehat{=}$ plane of incidence) and the sagittal plane [66]

$$f_s = \frac{R}{2}\frac{1}{\cos\varphi},$$

$$f_t = \frac{R}{2}\cos\varphi.$$

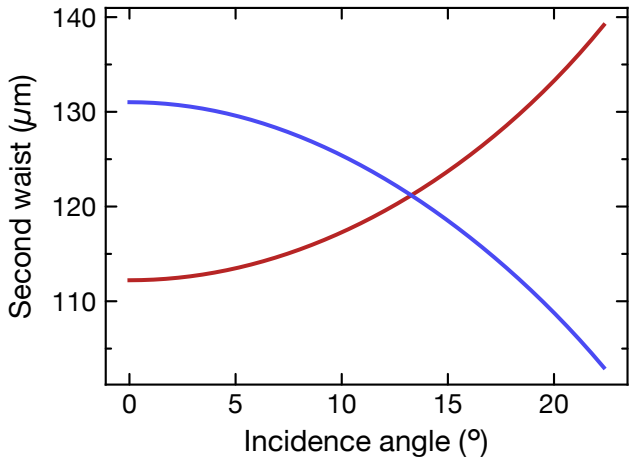

Figure 3.5 – Waist of the long arm depending on the incidence angle. The red (blue) line show the sagittal (tangential) waist in the long arm depending on the angle of incidence on the curved mirrors. The crossing of the curves corresponds to a round waist in the long arm.

The astigmatism of the mirrors and the Brewster cut can be used to compensate each other. However it is only possible to cancel the astigmatism in a full roundtrip, but it is not possible to achieve a round waist everywhere in the cavity. One possibility is thus to achieve a round waist in the crystal, matching it to the calculated waist in both planes. This seems desirable in terms of an optimal conversion efficiency, but comes with a disadvantage. A round waist in the crystal means a strongly elliptical waist in the center of the long arm. In practice this makes efficient incoupling to the cavity problematic, because the mode of the incoming beam has to be matched with the cavity mode. For this reason the waist in the crystal is not chosen to be round in this project.
Figure 3.5 shows the waists in the sagittal and tangential plane in the long arm depending on the angle of incidence on the curved mirrors. To aim for good incoupling, an angle is chosen that leads to an approximately round waist in the crystal. The corresponding full opening angle is $2\varphi = 30.01°$.
The waist in the tangential plane is thus slightly stretched as compared to the value calculated in Section 3.1.4, while the sagittal waist stays with the calculated value. Accepting this ellipticity in favor of a round incoupling beam has been tested and approved in various other works before [60, 62].

3.2.3 Impedance matching

To get the best possible conversion efficiency, the cavity has to be impedance matched. This means that the incoupled power has to be matched with the round trip losses. Besides the desired conversion to the second harmonic there are other sources of round trip loss. The reflectivity of the highly reflective mirrors R_2, R_3 and R_4 is not per-

fect, there might be absorption in the crystal, reflection on the surface of the crystal or even dust and misalignment. Those have to be estimated and mapped to the incoupled power. Perfect impedance matching is achieved, when the reflection of the incoming beam at the incoupling mirror and transmission of the circulating beam at the incoupling mirror are equal. If the light frequency matches the cavity resonance, the reflected incoming and transmitted circulating beam are phase shifted by 180° and interfere destructively. In the case of perfect impedance matching the incoming beam is fully coupled in the cavity because the reflection is canceled.

This can be calculated using the self-consistency requirement for the circulating field after one round trip [67]

$$\mathcal{E}_{\text{circ}} = i\sqrt{T_1}\mathcal{E}_{\text{in}} + g_{\text{rt}}(\omega)\mathcal{E}_{\text{circ}},$$

where $\mathcal{E}_{\text{circ, in}}$ are the circulating and incoming electric field amplitudes, T_1 is the transmittivity of the incoupling mirror and g_{rt} is the round trip function given by

$$g_{\text{rt}} = \sqrt{R}\, e^{-i\omega L/c}\, \sqrt{\alpha},$$

with L being the total optical length of the resonator, $R = R_1R_2R_3R_4$ being the reflectivity of all mirrors and α accounting for other losses. Assuming the length of the cavity to be on resonance with the frequency of the light field all the complex factors can be dropped. The power of the generated second harmonic can then be calculated as

$$P_{\text{SH}} = \kappa_{\text{NL}} P_{\text{circ}}^2$$

and accordingly the efficiency of the process as

$$\eta_{\text{eff}} = \frac{P_{\text{SH}}}{P_{\text{in}}}.$$

For perfect impedance matching the efficiency has to be optimized with respect to the incoupling mirror reflectivity. This depends on several factors, like the reflectivity of the other mirrors, the additional losses and the power of the incoming fundamental. They all have to be estimated in order find a suitable value for the input reflectivity. The estimations taken in this work are highly reflective mirrors of $R_2 = R_3 = R_4 = 99.95\%$, as given by the supplier Layertec, and additional losses of 0.5% [43]. The power of the fundamental is given by a tapered amplifier, specified for a 2 W output power. Here it is assumed that half or less of the TA output is available in the Gaussian mode. Figure 3.6 shows a plot of the efficiency depending on the input reflectivity with the given estimations. The curve is plotted for different fundamental powers of 0.5 W, 0.8 W and 1.1 W, which are the lower and upper limits of what is expected to be possibly coupled in to the cavity. Also in the plot are for each curve the maximum efficiency reachable [68]. The value for the input reflectivity that has been chosen is $R_1 = (98.8 \pm 0.1)\%$. It is slightly on the left of the optimum because of the sharp drop in efficiency on the right hand side of the maximum, where the cavity is undercoupled. In the figure this is shown as a shaded areas, indicating the reflectivity value within its error bars. In table 3.2 the efficiency, power of the second harmonic

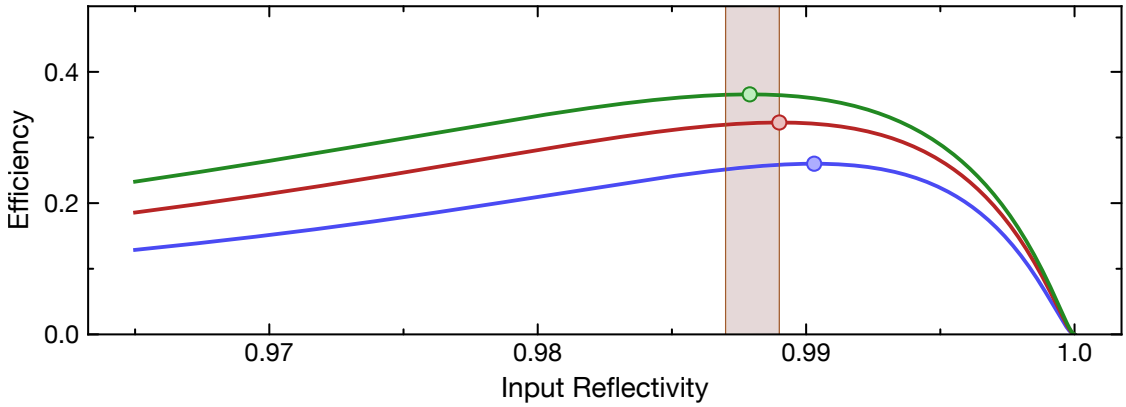

Figure 3.6 – SHG efficiency on incoupling reflectivity. Efficiency of the second-harmonic generation depending on the reflectivity of the incoupling mirror. The blue line represents the case of 0.5 W power of the fundamental wave, the red represents 0.8 W and the green 1.1 W. The dots indicate the maximum of efficiency for each line, the shaded area centered around 98.8% reflectivity marks the value of the input reflectivity within its uncertainty that was chosen for the cavity

P_{in} (W)	η_{eff} (%)	P_{SH} (W)	P_{circ} (W)
0.5	30	0.151	57
0.8	37	0.299	79
1.1	42	0.460	97

Table 3.2 – Efficiency, power of the second harmonic and circulating power. For different powers of the fundamental the efficiency, power of the second harmonic and circulating power in the cavity are shown for the chosen input reflectivity of 98.80% and additional losses of 0.5%.

and circulating power are listed for the different input powers with the selected input reflectivity of 98.8%.
With these values the doubling cavity is determined in its geometry. The beam waist has been calculated as $\sqrt{3}$ times the optimum given by the Boyd-Kleinman optimization in order to prevent thermal lensing. The geometry of the enhancement cavity was determined by the stability condition and the decision for a round waist in the incoupling path. Finally the reflectivity of the incoupling mirror is chosen to optimize impedance matching. Table 3.3 sums up the final cavity geometry and the specification of the different elements.

Quantity	Value
nonlinear coefficient κ_{NL}	$4.9 \times 10^{-5}\,\mathrm{W}^{-1}$
crystal length l	10 mm
temperature T	82°C
crystal waist saggital $w_{\mathrm{c,s}}$	41.9 µm
crystal waist tangential$w_{\mathrm{c,t}}$	64.3 µm
second waist saggital $w_{2,\mathrm{s}}$	123.7 µm
second waist tangential $w_{2,\mathrm{t}}$	118.5 µm
mirror curvature R	50 mm
full opening angle 2φ	30.01°
short arm d	56.8 mm
long arm d	147.8 mm
input reflectivity R_1	98.80%

Table 3.3 – Geometry for the SHG Cavity. Final geometry and other specification for the cavity.

CHAPTER 4

Experimental setup – design and characterization

This chapter reports on the design and characterization of the laser system. The setup is first sketched out in its most relevant components and then discussed in detail. The NIR 980 nm setup is described including the design of the home-built Littrow lasers and tapered amplifiers. The stabilization of the laser to a ULE cavity is characterized. As for the blue 405 nm setup, the emphasis will be on the design and characterization of the doubling cavity. The frequency stabilization through a transfer cavity is characterized including the laser lock and the stabilization of the cavity length.

4.1 Overview

The two-photon setup consists of two parts. In the 405 nm setup, referred to as *blue setup* from here on, coherent, frequency stabilized 405 nm laser light is created, which can drive the 4S to 5P transition in ^{39}K. The *NIR setup* generates near-infrared (NIR) 980 nm laser light, frequency stabilized to a ULE cavity, which drives the 5P to nS transition and can be tuned in wavelength to address almost all of the available Rydberg states.
Figure 4.1 shows a general scheme of both the blue and the NIR setup. The NIR setup begins with an external cavity diode laser (ECDL), which will throughout the chapter be referred to as the 980 nm laser, since it can be tuned by several nm to all Rydberg states around that value. After an optical isolator, the light is sent into a tapered amplifier (TA), and after another optical isolator passes an AOM and then gets coupled into a fiber. Before the amplification stage a small fraction of the light is used for frequency stabilization. For that a fiber coupled electro-optic modulator (EOM), driven by a local oscillator, generates sidebands on the light, which is then coupled to an ultra low expansion (ULE) cavity. The reflection is used to stabilize the frequency of the light.
The blue setup begins with an near-infrared laser at 810 nm that is amplified using a TA. The light is then coupled to a doubling cavity where it is frequency-doubled to 405 nm. Then it is sent through an AOM and gets coupled to a fiber. For frequency stabilization a small fraction of the light is split off the main beam and is sent through a fiber to a cavity. The sidebands for the Pound-Drever-Hall lock are created via current modulation of the laser. The reflection signal is used to stabilize the laser. The cavity is called a transfer cavity, because it is not stable by itself, but has to be stabi-

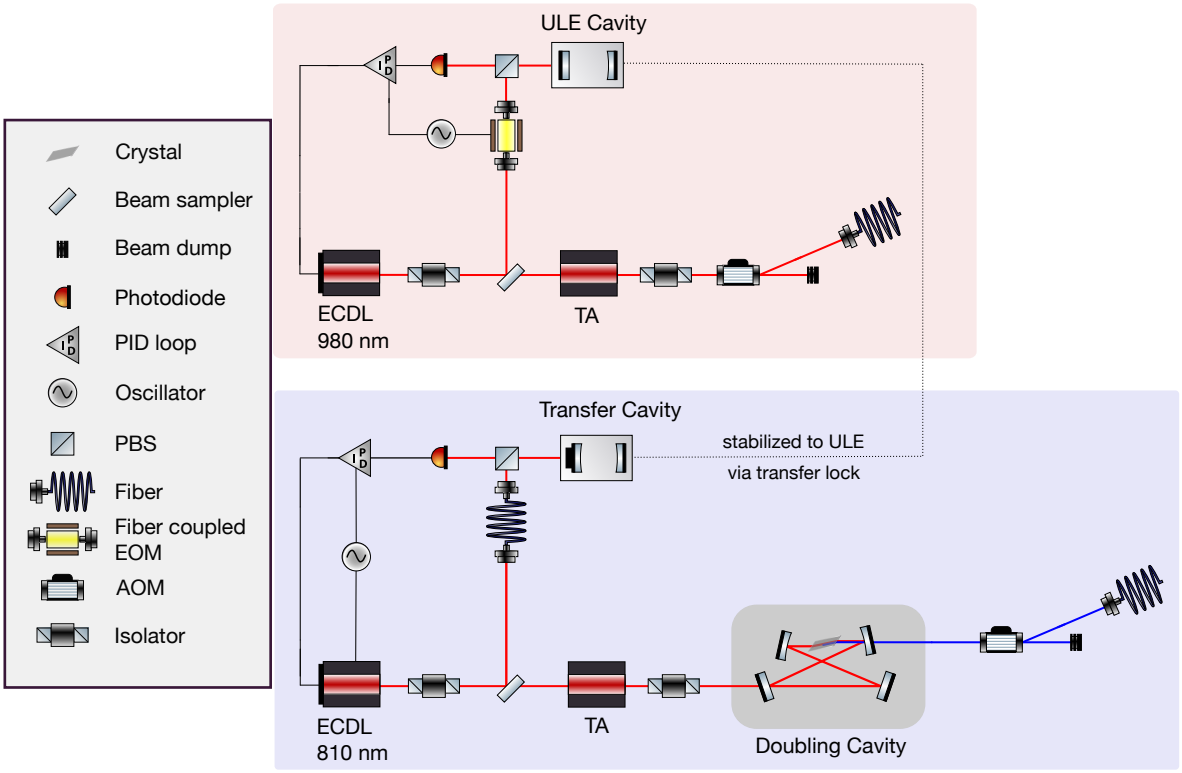

Figure 4.1 – Schematic of the two-photon setup. The complete setup including both the NIR and the blue setup is shown. The graphic only shows the most relevant elements. An overwiev over the setup is given in the main text.

lized in length. This in done by keeping it on resonance with another laser, which is locked to the ULE cavity. The dotted line in the setup indicates that the transfer cavity is thus stabilized to the ULE.

4.2 The NIR 980 nm setup

In this setup more than 500 mW coherent, frequency-stabilized laser light is created to drive the 5P to nS transition frequency in potassium. Figure 4.2 shows the setup in detail. The ULE lock is shown separately in Section 4.2.3.
The laser is set to a wavelength of 974.7 nm, corresponding to the 5P to 50S transition, but can be tuned to address both higher and lower states. The setup profits from a wavelength that is well suited for generating and amplifying laser light. Relatively broad laser diodes, that can cover the whole range of possible transitions from 5P to Rydberg states, are commercially available and tapered amplifiers that can provide 2 W or even more in this frequency regime are widely used and have proven to be reliable.

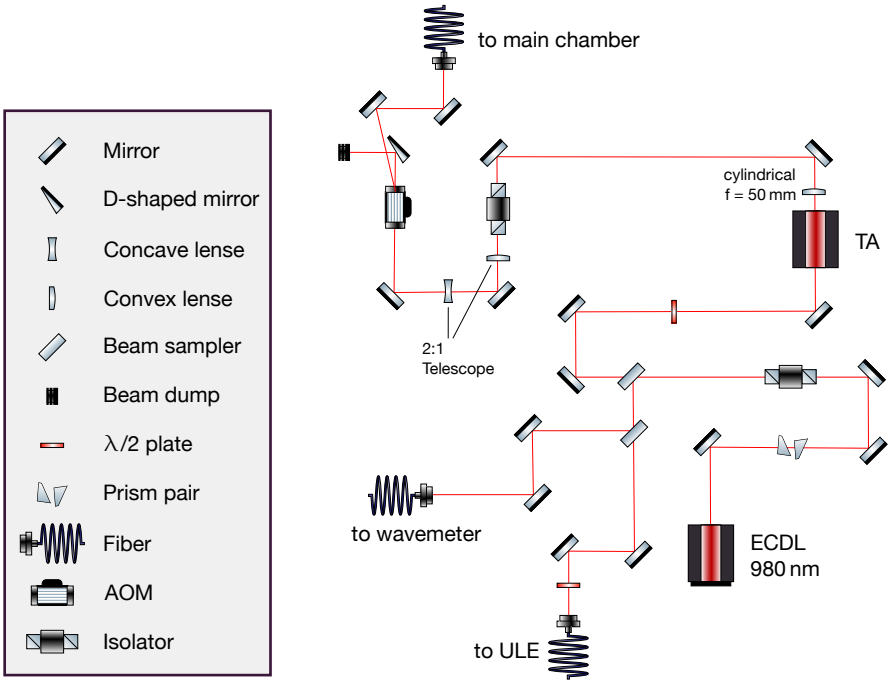

Figure 4.2 – NIR laser setup. The figure shows the detailed setup for the NIR laser with ECDL, TA, AOM and fiber coupling, but without the setup of the locking, which is shown in its respective section.

4.2.1 The external cavity diode laser at 980 nm

An external cavity diode laser consists of a diode and an element outside of the diode housing which, together with the diode, defines a cavity. Only frequencies resonant to the cavity can propagate in the cavity, while all other frequencies vanish. Through stimulated emission the diode amplifies the propagating frequencies. Since the gain profile of a diode varies with frequency, one of the modes that is selected by the cavity gets most amplified and dominates the output. The desired case is to have the diode emitting in a single mode, such that all other frequencies are suppressed by the most dominant one. In order to change the wavelength of the laser, an additional element of selection needs to be included, which allows only a small range of the whole gain profile to be fed back to the diode. The dominating frequency can then be adjusted by changing the location of this range in the gain profile.
In this thesis a Littrow laser is built, where a grating is used to select a frequency range [69]. The grating is a dispersive element, reflecting light in a frequency-dependent angle. By changing the angle of the grating one changes the frequency range that gets reflected back in the diode giving it feedback. The grating functions as a frequency selection but also defines a cavity through the distance between grating surface and diode. This allows for tunable single mode operation of the diode. A part of the light is reflected back towards the diode, and the rest gets reflected under an angle such that it leaves the ECDL.

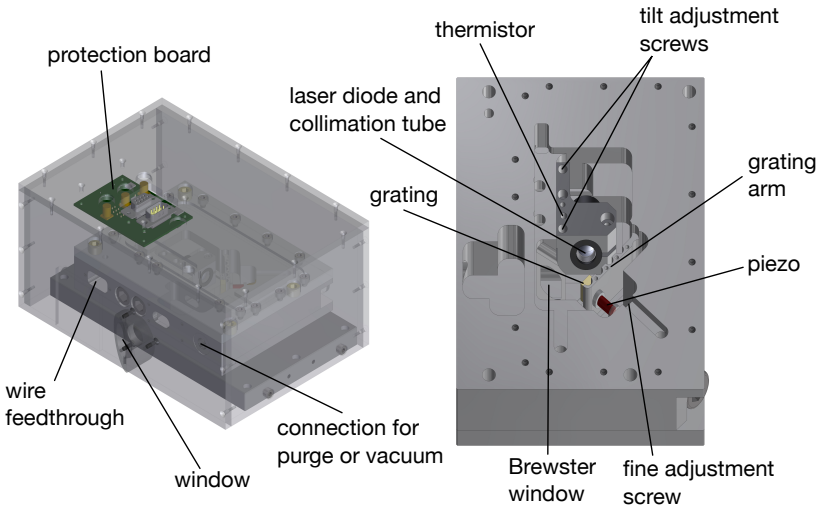

Figure 4.3 – Design of the Littrow laser. The design of the home built Littrow lasers is shown. On the left side the aluminum housing of the laser inside an acrylic glass housing. The inside of the laser is shown on the right. The collimation tube with the diode can be adjusted in position with the tilt adjustment screws. The grating is glued on the grating arm and can be adjusted in angle using the fine adjustment screw. The piezo mainly affects the cavity length through slightly pushing the grating arm and has negligible effect on the angle. The thermistor measures the temperature close to the diode, which is fed back to two Peltier devices located at the bottom of the aluminum housing through a PID loop. The solid aluminum housing is air-tight and allows for evacuation of the laser.

Littrow laser design and assembly

The particular design for this Littrow laser is adapted from the Steck group at the University or Oregon [70]. In Figure 4.3 a render of the design is depicted. Laser diode and grating are fixed in a solid block of aluminum and the grating angle is set adjusted via the grating arm. The diode sits in a collimation tube which contains a lens in adjustable distance to the diode. The aluminum housing is further protected against disturbances from the environment via an acrylic glass enclosure and is temperature stabilized using two Peltier devices. The design allows for evacuation of the interior of the laser, which has however not been carried out for the lasers in this setup.
The position of the grating has to be roughly set using the adjustment screw before the position of the diode can be fixed. The position of the diode is crucial for the laser to stably lase, because a slight tilt in the wrong direction can lead to the feedback beam not hitting the diode properly. The lasing threshold then decreases drastically or even vanishes completely. When the grating is moved considerably, the reflected beam also changes in position and the diode has to be adjusted all over. It is thus useful to calculate the expected angle of the grating for a desired wavelength. The angle dependence is given by

$$2a\sin(\theta) = \lambda,$$

where a is the grating spacing. This means that at angle θ the wavelength λ gets the biggest gain from the grating. For a wavelength of 980 nm and the used grating of 1500 grooves per millimeter, an angle of 47.31° leads to an optimum gain. This is slightly bigger than the 45° the Littrow lasers are designed for and in fact is on the edge of the beam still being able to leave the housing without clipping on the housing. However the laser might still lase at a wavelength different from the gain peak of the grating, since the gain profile of the diode can be drastically different, such that the multiplied gain can have a shifted maximum. It might thus be that the grating has to be turned further away from the optimum gain, leading to a total suppression of the higher gain frequencies of the diode, but also to a considerable suppression of the desired wavelength and thus to a decreased output power and increased lasing threshold. It is thus best to use a diode which has its gain profile centered around the desired wavelength.
A broad, anti-reflection (AR) coated diode is used to prevent the diode surface from forming an unwanted cavity. The protection board is home-built and allows for individual adjustment. The protection board also allows for current modulation for laser locking via a DC port, and for AC current modulation via an AC port, for example for generating sidebands on the frequency. The design of the board was part of another master thesis and can be found in [71]. The output of the Littrow laser typically has an elliptic beam profile. Therefore an anamorphic prism pair is used to squeeze the horizontal axis of the beam.

Characterization

To characterize the laser, its output power is measured right after the housing. A measurement of the total output power indicates where the lasing threshold is, what the maximum output is and how steep the slope is. For working with the setup it is however more important to know the power that arrives at the TA, because the TA is sensitive to the seeding power. Thus Figure 4.4 shows both, the total laser output and the power that arrives at the TA, after a fraction of the beam has been split off for the lock and the wavemeter. The power does not rise completely linearly with increasing current. This is because the wavelength is slightly dependent on current. When increasing the current, at some point there is a mode jump and the new mode might be worse or better in terms of gain from the grating or the diode. This leads to the intensity curve deviating slightly from a linear slope.
Overall this laser provides enough power for the lock, the wavemeter and the seeding of the TA. It is currently set to lase at 974.7 nm, which corresponds to the 5P to 50S transition. This decision was made because at this wavelength the diode was observed to perform best. The gain profile is favorable for this wavelength, which leads to a stable output and the angle given by the grating is not as strong as for lower Rydberg states. It runs in single mode operation quite stably and can be scanned over several GHz without mode jumps. The wavelength can be changed by about 10 nm in both directions, though at about 985 nm, the angle of the grating will lead to the beam being clipped at the edge of the housing.

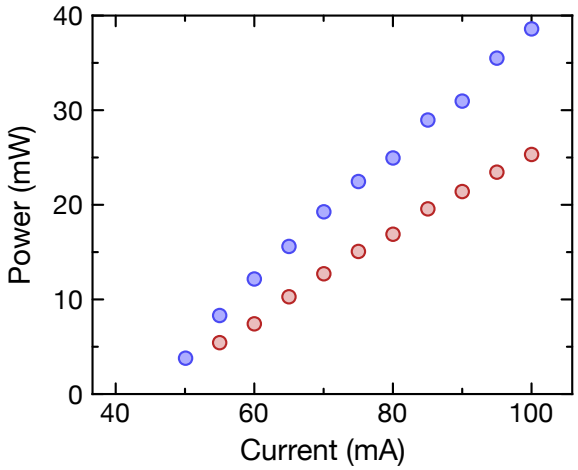

Figure 4.4 – Output power of the 980 nm Littrow laser. The plot shows the output power of the laser (blue) and the power at arrives at the TA for seeding (red).

In free running mode these kind of Littrow lasers have shown to be relatively sensitive to acoustic noise, probably due to the grating arm amplifying vibrations of the body. A solution could be to move the connecting point of housing and grating in line with the laser light, such that vibrations cannot affect the relative position between diode and grating so much. For that discussion also compare this Littrow laser design to the alternative (linear) laser design of Appendix B.

4.2.2 The tapered amplifier

The output of 40 mW from the ECDL is not enough to reach the Rabi frequencies aimed for in this project. An amplifier is needed. A cost-efficient way to amplify laser light in the range of 650 - 1000 nm is to use a tapered amplifier (TA). Such a TA consists of a tapered gain region of a semiconductor material, such as GaAs. Similar as in a laser diode, the electrons in the material get pumped in the conducting band when a current is applied. Without any further input spontaneous emission leads to fluorescence of the material. But if the chip is seeded by another laser in the right frequency range, stimulated emission takes place throughout the medium and amplifies along the tapered region, such that gains of a factor of 100 and more of the seeding power can be achieved.
In Figure 4.5 the TA chip and its mount can be seen. The housing has thread in the middle so the mount can be fixed onto a proper holder for the setup. While the housing forms the anode and gets grounded, the cathode sticks out on top of the mount and can be soldered to a wire or a connector. Right next to the long cathode, also on top of the mount, sits the TA chip, connected with thin, very sensitive wires. The TA chip has an entrance facet with a channel that allows only for a single mode, improving the seeding of the medium. Input and output facet are AR coated.

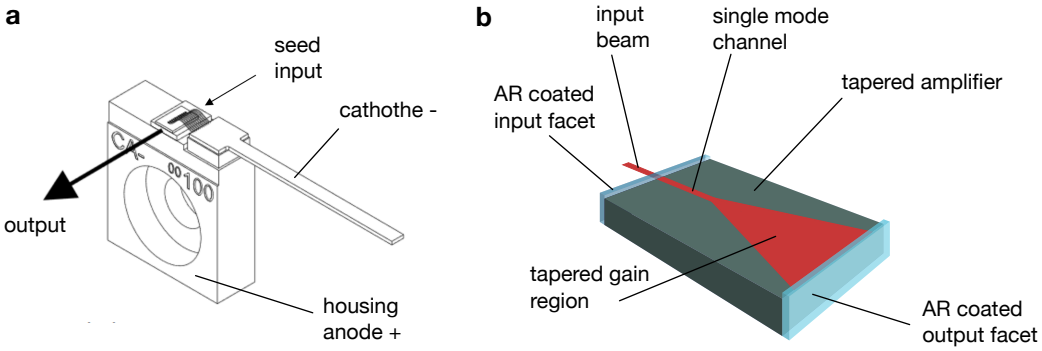

Figure 4.5 – TA chip and its mount. In **a** the mount of the TA chip is shown. The graphic is adapted from the Eagleyard datasheet [72]. In **b** a schematic of the chip with its tapered gain region is shown.

Design

The TAs used in this setup are commercially bought TA chips, mounted to a structure that has been designed in our group. Figure 4.6 shows this design. The TA chip in its mount is screwed on a copper mount, which is temperature stabilized using two Peltier devices. A thermistor right next to the chip reads the temperature. To carry away the heat produced by the chip, the copper plates next to the Peltiers are water cooled. There are two lenses, one to focus onto the chip and one to collimate the output. Both are fixed on a translation stage for optimal adjustment. Everything is protected from the environment by an acrylic glass housing. For current supply and temperature stabilization a protection board similar to the one for the ECDL, but without modulation ports, is used.

Beamshaping

While the input to the TA is not very demanding and basically only needs the right polarization and position of the focusing lens, it can be quite challenging to handle the output beam. The collimation lens inside the TA housing can only collimate the vertical axis, while the horizontal one remains strongly diverging. This is due to the tapered shape and the horizontally stretched output facet. To collimate this axis, a cylindrical lens is needed, where the right focal length has to be found by testing. After successful collimation of both axis the beamshape is still far from a Gaussian. Instead it has a rectangular, inhomogeneous shape of superimposed roundish beams. In order to fit the beam through an isolator it has to be reduced in size using a telescope consisting of two lenses. The non-Gaussian portion of the beam then slowly diverges and after half a meter to a meter after the TA the beamshape resembles a Gaussian.

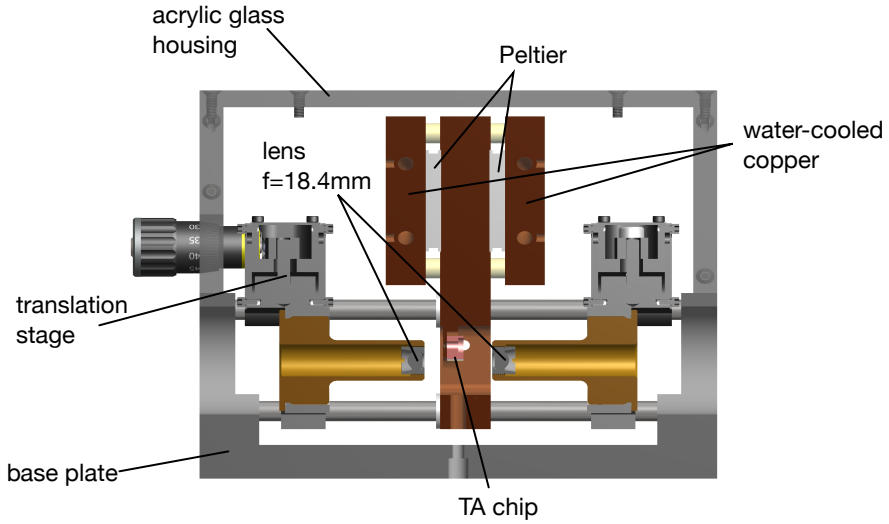

Figure 4.6 – Design of the TA. The design for the tapered amplifiers with the copper mounts, Peltier devices, translation stages for the lenses and the surrounding acrylic glass is shown. The upper copper plates have copper tubes with water flow going through which carry heat away.

Characterization

In case of sufficient seeding of 15 mW to 25 mW and good coupling, the output of the TA depends roughly on three parameters, namely the temperature of the chip, the seeding power and most importantly the current applied to the chip. In Figure 4.7 the output of the TA depending on current and seeding is shown. Up to a current of roughly 700 mA no considerably amplification takes place. From there the output power shows a linear increase with current. The maximum output at the maximum rating of 3.5 A is slightly above the specified output of 2 W. However, since the isolator in the setup is specified with a maximum of 1.7 W, the TA can not be used at its maximum power anyway. A comparison of the different seedings in the same figure shows that the saturation point for the seeding is current dependent, such that the output is not always saturating at 20 mW. Higher seeding is not measured, since more than 25 mW may decrease the lifetime of the TA.

The temperature dependence of the output power is shown in Figure 4.8. One would expect a curve with a clear maximum at a certain temperature and a slow decrease in power to both sides of the maximum, as in [73]. The figure indeed shows an increase towards lower temperatures. Even lower temperatures were not not tested because below 15°C condensation could damage the TA chip. Despite the monotonous growth in power, the curve does not look as smooth as expected. To investigate this behavior a measurement on a much smaller temperature scale was taken. This shows that on a scale of about 0.4°C the power oscillates in a sine shaped manner. This oscillation explains the behavior on the bigger scale, since random points along this oscillation are taken in the measurement. The small scale oscillation could be explained by two imperfectly AR coated facets that form a cavity. A change of temperature leads to the

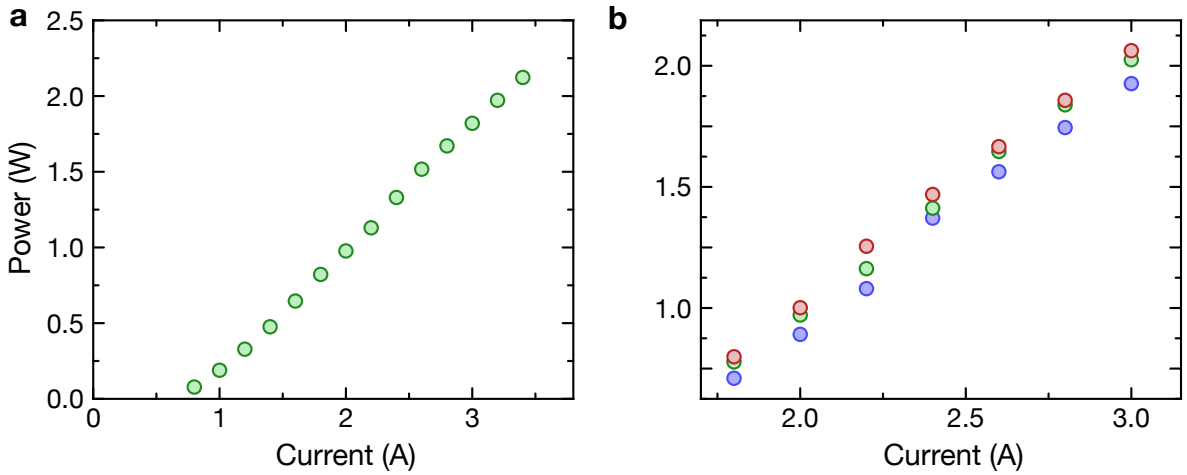

Figure 4.7 – 980 nm TA output on current. Figure **a** shows the TA output for 20 mW seeding power and **b** shows the output for 15 mW seeding (blue), 20 mW seeding (green) and 25 mW seeding (red).

expansion of the medium, which changes the resonance of the cavity and thereby the suppression of the output.
Before the light gets coupled into a fiber, it is send through an AOM (Gooch & Housego AOM 3110-197). This allows both for fast switching on and off the light and for precisely scanning a frequency range of a few MHz. The peak efficiency achieved with the AOM in this setup is less than 60%. Figure 4.9 shows the output of the AOM in the first order for an input of about 150 mW. Instead of a curve with one clear optimum, the AOM has a second, local maximum about 10 MHz from the global maximum. A very similar behavior with comparably bad coupling has been found in our lab with the AOM 3110-120 in [74]. In both cases optimization failed despite several attempts to improve. The reason has not yet been found.
The zero order output of the AOM is picked up using a D-shaped mirror and set to a beam dump. The first order output of the AOM gets coupled into a fiber with 70% efficiency. The total efficiency from the TA to the fiber output, due to losses from the TA beamshaping, the isolator, the AOM and the fiber coupling, are about 36%.

4.2.3 Locking to the ULE cavity

For the final experiment the laser light has to be stable in frequency, both long term and short term. Long term stability is necessary for the experiment to provide reproducible results. Short term fluctuations of the frequency affect the coherence time of the atoms and the frequency resolution of measurements. Thus the laser should be frequency stabilized with a small linewidth and good long term stability.
In this setup the laser is frequency stabilized to a cavity. The length of the cavity serves as a reference for the wavelength of the laser. When the laser is resonant on the cavity length, a standing wave builds up inside the cavity. The circulating power in the cavity then is so large, that the transmission through the mirrors is detectable. Behind the

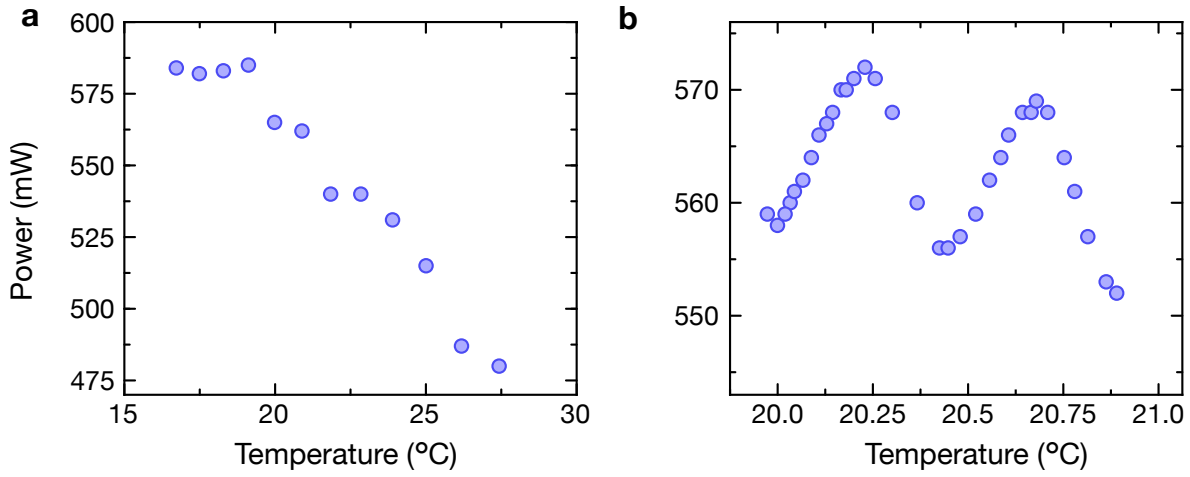

Figure 4.8 – 980 nm TA output on temperature. Figure **a** shows the output power for several temperatures between 15°C and 30°C. Figure **b** is measured on a shorter scale, ranging only from 20°C to 21°C.

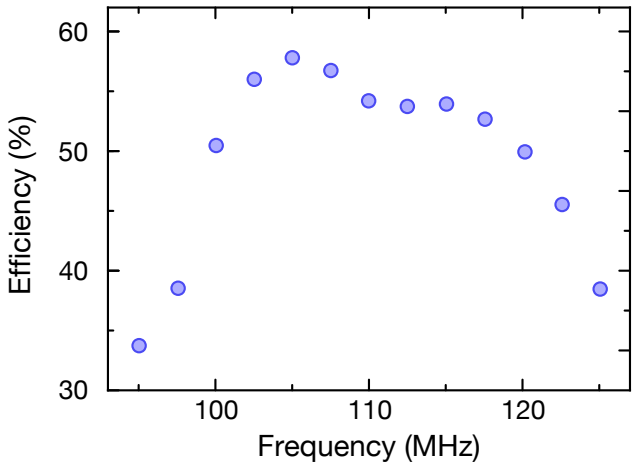

Figure 4.9 – AOM output power on frequency. The output of the AOM in the first order is plotted for different driving frequencies of the AOM.

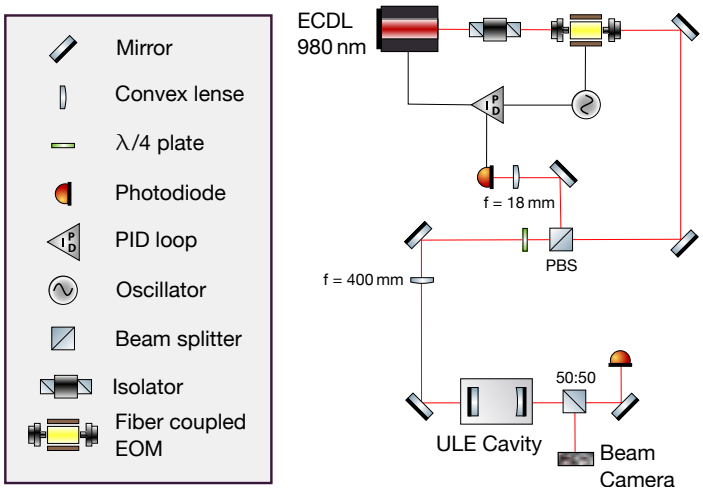

Figure 4.10 – Schematic of the ULE lock setup. The figure shows the detailed setup of the ULE laser lock. A fiber EOM is used for phase modulation. While the transmission is monitored to make sure to lock on the right mode, the actual error signal is generated using the reflection signal, which is split from the incoming beam using a $\lambda/4$ plate and a polarizing beam splitter (PBS).

cavity a transmission signal can be seen, whereas the back reflection from the cavity shows a considerable decrease as compared to the non-resonant case, because the circulating light transmitted through the input mirror is 180° shifted in phase regarding the input and thus destructively interferes with the reflection.

Figure 4.10 shows a schematic of the setup for the lock to the ULE cavity. The EOM is a fiber coupled EOM from EOSPACE (model PM-0S5-10-PFA-PFA-970/1005) that is suitable for all modulation frequencies from DC to 10 GHz. This is needed for the specific locking in this setup, where two sideband frequencies are used to lock the laser on a frequency independent of the cavity resonances, as discussed later in this section. The transmission photodiode and camera are used to monitor the transmission and make sure the right mode is used for locking. The photodiode is home-built, information on the circuit can be found in [71]. The signal of the reflection photodiode is used for locking the laser. Further explanations about the locking procedure follow later in this section.

Ultra low expansion cavity

In this project an ultra low expansion (ULE) cavity is used. The cavity mirrors are coated for three different wavelengths, namely 1142-1162 nm, 970-998 nm and 765-775 nm. The mirrors are optically contacted to a 10 cm long spacer out of ultra low expansion glass, ordered from Advanced Thin Films. Although not at its zero expansion point in this setup, the material shows very little length dependence on temperature. Low expansion is an important property, because length fluctuations are related

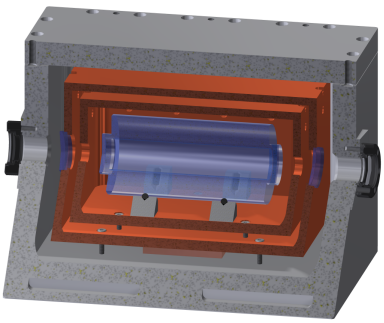

Figure 4.11 – ULE vacuum chamber. The design of the vacuum chamber to shield the ULE cavity is shown. Inside lies the ULE glass with the mirrors, protected by the inner and outer copper shield and surrounded by an aluminum chamber.

to frequency fluctuations as

$$\frac{\Delta\nu}{\nu} = \frac{\Delta L}{L}.$$

For 980 nm this yields

$$\frac{\Delta\nu}{\Delta L} = 3\,\mathrm{MHz/nm}.$$

It is thus crucial to keep length fluctuation as low as possible. The cavity is thermally and vibrationally shielded by two copper shieldings which are actively temperature stabilized using only one Peltier device. This design is inspired by [75]. The cavity with the shieldings sits inside an aluminum vacuum chamber with slightly tilted viewports. A render of the shieldings and the chamber with the cavity inside can be seen in Figure 4.11. Further information on the vacuum system and temperature stabilization and further uses of the ULE cavity in our potassium experiment can be found in [76].

In order to optimally couple into the cavity, the geometry of the incoming beam has to be matched with the cavity mode. The geometry of the TEM_{00} mode can be calculated using Gaussian beam optics, as done for example in [77]. The radius of the curvature of a beam can be calculated as

$$R(z) = z\left(1 + \left(\frac{\pi\omega_0^2}{\lambda z}\right)^2\right),$$

where z gives the position along the axis of propagation and ω_0 is the beam waist at the $z = 0$ position. The resonance condition for the cavity states that the radius of the beam curvature has to equal the radius of the mirrors at the mirror position. In the ULE cavity in this setup the first mirror is flat and thus falls together with the position of the beam waist. The second mirror has a curvature of $R_2 = 50\,\mathrm{cm}$, and

thus $R(L) = 50\,\text{cm}$. This can be solved for

$$\omega_0 = \sqrt{\frac{\lambda\sqrt{RL - L^2}}{\pi}} = 248.5\,\mu\text{m}$$

and

$$\omega(L) = \omega_0\sqrt{1 + \left(\frac{L\lambda}{\pi\omega_0^2}\right)^2} = 278.4\,\mu\text{m}$$

The collimated beam after the fiber has a a diameter of 760 µm, measured using a camera (VRmC-9+/BW-OEM, VRmagic) and fitting a Gaussian to the beamprofile. The beamdiameter then is given as the diameter where the beam has $1/e^2$ of its peak intensity. A convex lens of focal length $f = 400\,\text{mm}$ in a distance of 230 mm from the first cavity mirror matches the beam onto the cavity mode.

Characterization of the cavity

The longitudinal modes of the cavity are spaced in frequency depending on the length of the cavity. The frequency range after which the resonance peaks of the cavity repeat is called the free spectral range (FSR). It is given by

$$\Delta\nu_{\text{FSR}} = \frac{c}{2L} = 1.5\,\text{GHz}.$$

In order to achieve the best possible signal, the incoupling mirrors have to be adjusted such that the Gaussian mode TEM_{00} is the dominating resonance peak, ideally such that all other modes are completely suppressed. Figure 4.12 shows the transmission signal for a frequency scan over the free spectral range. The data have been taken using a TektronixDPO 2024B 200 MHz oscilloscope, as all the oscilloscope data in this thesis. It can be seen in the plot that there is one dominating peak and only one other, minor peak. The dominating peak is the TEM_{00}, the other peak is a superposition of the TEM_{01} and TEM_{10}. This has been checked using the camera in the setup.
To measure how much of the incoming beam is actually coupled into the cavity, one has to look at the reflection signal. At the resonance frequency the reflection shows a drop. The drop of this signal is equal to the amount of incoupled light. Figure 4.12 also shows the reflection signal for a frequency scan over the resonance peak. While the transmission signal of the last figure only shows structureless lines, in this case the dip is much more resolved. This is due to the frequency scale, being about a factor of a thousand different. The reflection in this plot is normalized such that the offresonant reflection level is set to 1. Then it can be simply read from the graph that about 80% of the light are coupled into the cavity.
Besides some noise in the reflection signal, the scan also shows a peak right after the incoupling dip. This peak arises due to the high finesse of the cavity. The reflection of the mirrors is so high, that the light gets stored for a short time inside the cavity. When the frequency is not on resonance any more, there is still a standing wave inside the

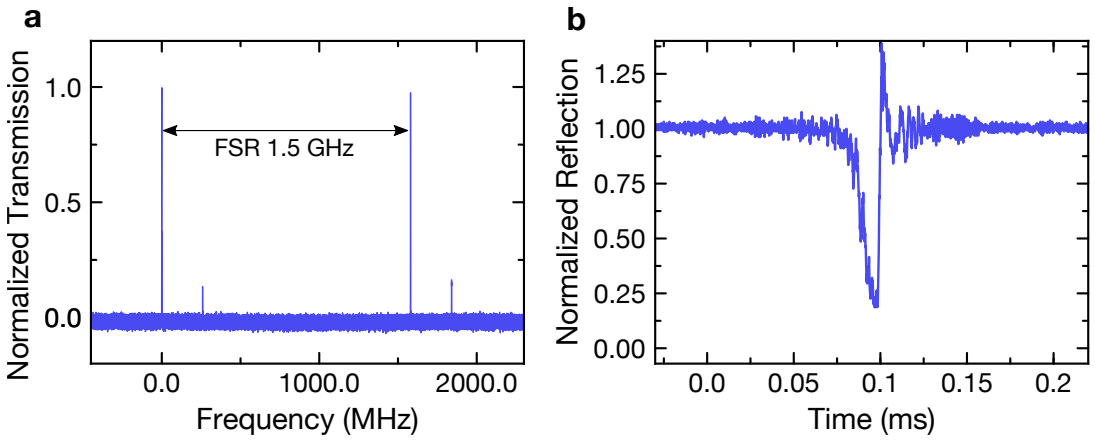

Figure 4.12 – ULE free spectral range and incoupling. In **a** the transmission signal can be seen when the frequency is scanned over the full FSR. After the free spectral range the signal repeats itself. The frequency scale is set using the calculated free spectral range and not known from the measurement itself. In **b** the reflection signal is shown. The dip corresponds to one of the high peaks of the transmission signal but on a much shorter frequency scale. Since only the peak is scanned no reference can be used to set the right frequency scale.

cavity leading to transmission on both cavity mirrors. This additional light interferes with the reflected light and is seen as a decaying oscillation, called ringdown.
The finesse of a cavity is defined as the FSR divided by the FWHM of the peak intensity

$$\mathcal{F} = \frac{\Delta\nu_{\mathrm{FSR}}}{\Delta\nu_{\mathrm{FWHM}}}.$$

To determine the finesse of the cavity, a straight forward approach is thus to scan over the resonance peak and measure the width. The FSR could be used as a frequency reference, but the width of the resonance peak is four orders of magnitude smallers and its difficult to measure on a few kHz exact when scanning over 1.5 GHz. Thus small sidebands of 3 MHz are generated and used as a reference. Figure 4.13 shows the transmission for a scan over the resonance peak with sidebands of 3 MHz distance to the main peak. The scanning time was set slow enough such that the ringdown effect does not affect the shape of the transmission signal. The finesse measured with this peak is roughly $\mathcal{F} = 6000$. But it can be seen in the plot that jittering of the laser might have affected the lineshape, thus several measurements have been taken. By averaging the finesse is measured to be $\mathcal{F} = 7500 \pm 1400$. This high error means that the measurement gets highly affected by some random disturbances, in this case the large linewidth of the free running laser. This indicates that measuring the finesse in this way is not reasonable for very high finesse [78]. In the case of this ULE the finesse is not as high as in the cited work, but it is still high enough such that the linewidth of the free running laser is too high to allow for resolution of the cavity linewidth. Thus another technique has to be employed.

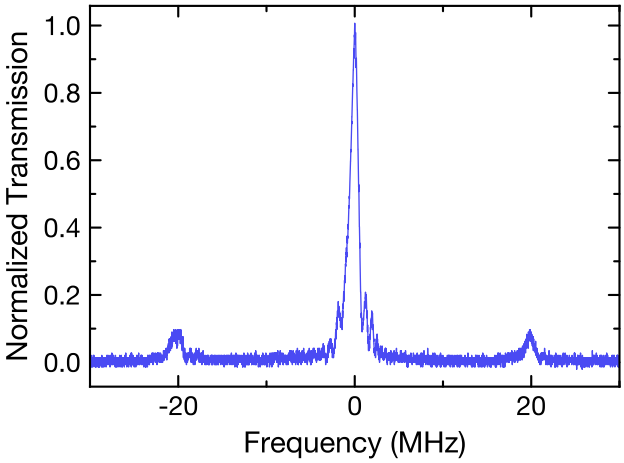

Figure 4.13 – Single transmission peak of the ULE. The figure shows a single transmission peak of the ULE cavity with its 20 MHz sidebands. The position of the sidebands is affected by a slight nonlinearity of the piezo used for the scanning and also by instabilities in the laser leading to frequency jumps during the scan.

The ringdown, which has already been mentioned in this section, also depends on the finesse and can be used to achieve a more accurate measurement [79]. The ringdown time τ is related to the finesse via

$$\mathcal{F} = \frac{\pi c \tau}{L}, \tag{4.1}$$

where τ is given through the exponential decay $U(t) = U_0 e^{-t/\tau}$ of the energy stored in the cavity. The ringdown time can be extracted from both the transmission and the reflection signal of a sweep over the resonance. Using the parametrized sweep rate

$$\nu_s = \frac{2\mathcal{F} d\dot{\omega} \tau_s}{\pi c},$$

where $\dot{\omega}$ is the laser frequency sweep rate (in units of radians per s^2), the transmitted and reflected signal can be expressed by

$$I_t(t) = \frac{\beta^2 I_0}{\nu_s} \left| \sqrt{\frac{\pi}{2}} e^{-t' + i\nu_s t'^2/2 - i/(2\nu_s)} + i\sqrt{2}\, D\left(\frac{i + t'\nu_s}{\sqrt{2i\nu_s}} \right) \right|^2$$

$$I_r(t) = I_0 \left| 1 - \frac{\beta}{\sqrt{\nu_s}} \left(\sqrt{\frac{\pi}{2i}} e^{-t' + i\nu_s t'^2/2 - i/(2\nu_s)} + \sqrt{2i}\, D\left(\frac{i + t'\nu_s}{\sqrt{2i\nu_s}} \right) \right) \right|^2,$$

for a sweep from the far off resonant over the cavity peak. Here the time has been normalized by $t' = t/(2\tau)$. Furthermore $D(x) = e^{-x^2} \int_0^x e^{\xi^2} d\xi$ denotes the Dawson

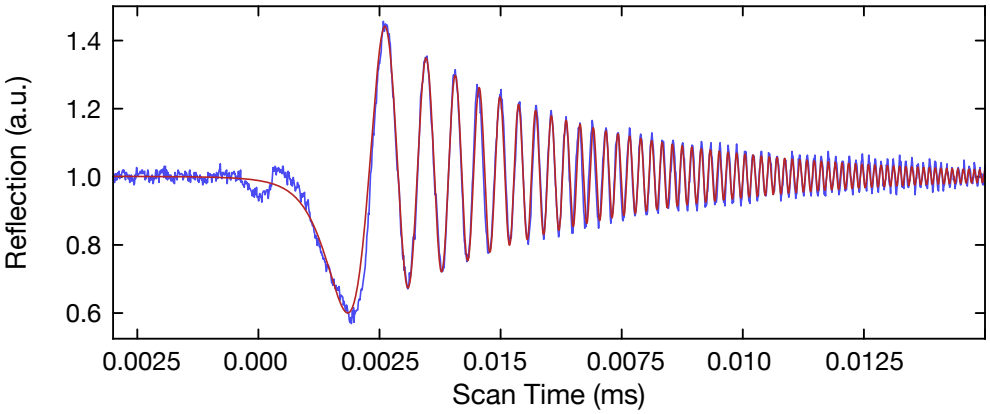

Figure 4.14 – ULE ringdown in the reflection signal. The plot shows the reflection signal for a fast scan over the resonance (blue). The ringdown oscillations can be seen clearly over more than 10 µs. The red curve is a fit of the theoretical ringdown curve to the data, giving a ringdown time of $\tau = (2.03 \pm 0.03) \cdot 10^{-3}$ ms. The theoretical curve matches the data very well and only deviates slightly for later times, when the ringdown effect becomes very small. This is most likely due to the noise in the signal.

integral and $\beta = T/(1-R)$ is the cavity contrast parameter.
Figure 4.14 shows a measurement of the reflection signal with a fit of the theoretical reflected intensity. The fit indicates in a ringdown time of $\tau = (2.03 \pm 0.03) \cdot 10^{-3}$ ms. Using equation 4.1 leads to a finesse of

$$\mathcal{F} = 19\,000 \pm 280.$$

In order to measure a ringdown signal which can be used for a fit, the sweep had to be much faster than in the scans before. This is due to several reasons. First, the laser may jitter during the scan and repeat the peak signal if scanned too slow. Second the oscillation must be clearly separated from the main peak, otherwise the linewidth of the laser again dominates the result. It turned out that the reflection is better suited for this measurement, since the peaks are more clearly separated. Also in this specific setup the photodiode for the reflection is better suited for measuring a fast sweep, because it has a larger bandwidth than the transmission photodiode. The reflection is used for locking and needs higher bandwidth while the transmission is only used for monitoring.
This measurement may overestimate the finesse nonetheless. The difference between the slow and the fast scan for the reflection show a significant difference in the deepness of the resonance dip. This indicates that either photodiode or the oscilloscope used to take the data are too slow to resolve the full size of the peak. In that case the ringdown time would be overestimated and with it the finesse. The theoretical value extracted from the transmission curve of the ULE mirrors given by the supplier indicates a finesse of 15 700 for 975 nm.

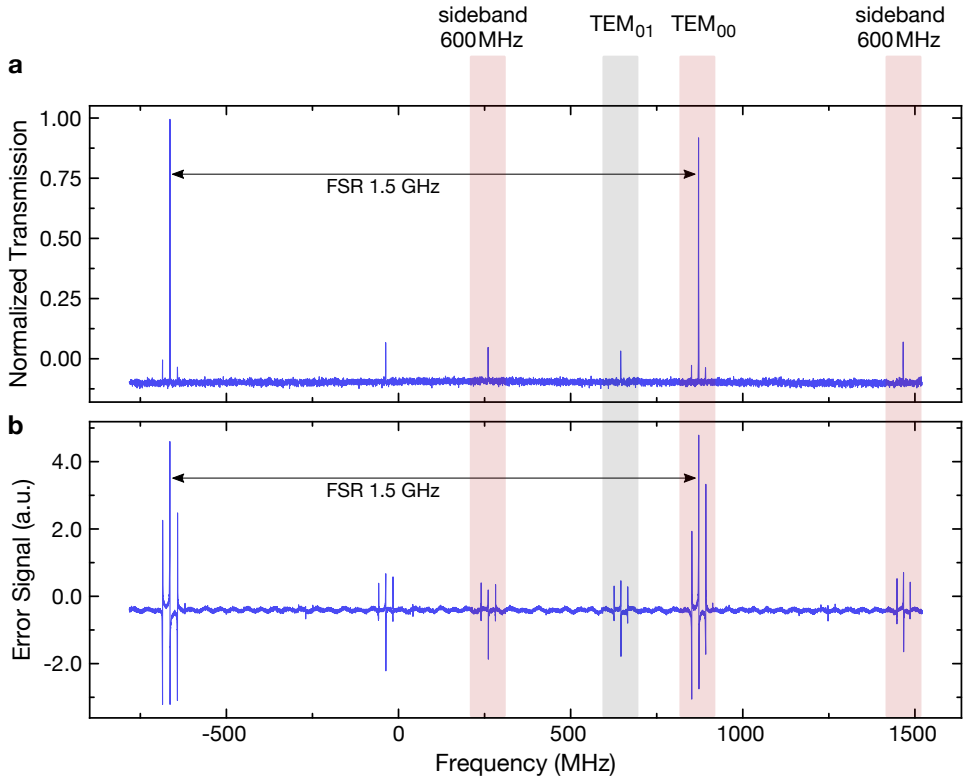

Figure 4.15 – ULE transmission and error signal. The ULE transmission (**a**) and corresponding error signal (**b**) is shown including both, the small 20 MHz and large 600 MHz sidebands. The sidebands of the TEM_{01} mode cannot be seen in the transmission and appear very small in the error signal.

Pound drever hall lock

The ULE cavity is used to frequency stabilize the 980 nm laser using the Pound-Drever-Hall method [80, 81]. Through phase modulation in an EOM, sidebands at ± 20 MHz are created on the laser frequency. Demodulation of the reflection signal at the modulation frequency yields the derivative of the original reflection signal, which is linear around the resonance and has a zero crossing right at it. Close to the resonance it thus serves as an error signal, being proportional to the frequency deviation from resonance. Through an electronic circuit this information is fed back to the laser to hold it at the resonance.
The NIR laser in this thesis has to be locked on the frequency resonant to the atomic 5P to 50S transition in potassium. The cavity resonances, on the other hand, are determined by the length of the cavity. In order to lock the laser on any frequency instead of the fixed resonance frequencies of the cavity, additional sidebands have to be created. Sidebands cause additional resonances of the light shifted from the carrier resonance by the modulation frequency. It is thus possible to lock to sidebands, using a second sideband frequency for demodulating the signal. The free spectral range of the used ULE is 1.5 GHz, thus sidebands of 0 to 800 MHz are needed to cover the full range

between the resonances and make it possible to lock to any frequency. In this setup a DDS (chip AD9910) referenced by an atomic clock is used to generate a stable oscillating signal at 0 to 400 MHz, which is then doubled and combined with the 20 MHz signal for the demodulation. The combined signal is fed to the EOM, which generates the sidebands on the light. A scheme containing the complete circuit can be found in Appendix A.
Figure 4.15 shows a scan over the free spectral range. The small sidebands are set to 20 MHz and the large sidebands are set to 600 MHz. The resonance peak of the Gaussian mode is dominating the signal. The small sidebands of the carrier can clearly be identified as well as the large sidebands, whose small sidebands are almost invisible. There also appears one other mode which is still slightly coupled into the cavity. The corresponding error signal can also be seen in the figure. Sidebands which are invisible in the transmission show up as clear peaks in the error signal.

Characterization of the lock

Generally the intensity for a ULE lock should be kept low in order to not heat up the cavity mirrors. In this locking setup a beam of 480 µW is send to the cavity. However most of the intensity is in the main peak and does not get coupled to the cavity when the laser is locked on the sidebands. Most of the intensity is thus reflected and less than 15 % of the total intensity is coupled to the cavity. The actual locking is done with 50 µW to 100 µW.
The resonance peak of a $\mathcal{F} = 19\,000$ cavity with 1.5 GHz FSR is less than 100 kHz sharp. Therefore fast electronics is needed to lock the laser. This setup uses a FALC 110 from Toptica for fast feedback, directly modulating the current of the laser diode with a signal path up to 100 MHz (-3dB bandwidth). For slower feedback a home-built lockbox is used. It modulates the piezo on the grating arm in the laser with up to about 1.5 kHz. This feedback is much slower than current feedback, but can compensate for slow drifts which are too large for compensation by current. While the slow box has a proportional (P) and integration (I) gain to adjust the feedback loop, the FALC also has a differential (D) gain to adjust.
Together the two lockboxes allow to stably lock the 980 nm laser to the ULE. To estimate the linewidth of the lock, the error signal of locked laser is measured using an oscilloscope. The error signal at each point in time corresponds to the difference between actual and resonance frequency. In order to assign a frequency error to the measured units of error signal, a frequency scan of the error signal is used. The frequency scan shows a linear slope of the error signal close to resonance. The distance to the sidebands of 20 MHz allows to identify the right frequency range of the slope, which can then be used to calibrate the recorded error signal units to frequency error. In Figure 4.16 the data for the linewidth estimation is plotted. Shown is a frequency scan with the sidebands, where the sidebands have been used to calibrate the x axis. A linear fit to the central peak gives the slope of the error signal. This allows to plot the error signal of the locked laser as frequency error on time, as shown in the figure. It shows the mean of the frequency and the standard deviation. The mean is not exactly zero, which originates from a slight offset the lock boxes receive and means that

the laser is stabilized to a frequency which deviated from the resonance peak by about 250 Hz. The linewidth is calculated with the standard deviation of the frequency as

$$\Delta\nu = 1.6\,\text{kHz}.$$

This linewidth has been calculated for a 1 ms time interval, but it does not change considerably when taking data over 10 ms or 0.1 ms. Only when going below 0.01 ms, the linewidth decreases by an order of magnitude, but in this range the oscilloscope's limits become relevant, such that better measurements have to be done to confirm or discard this short timescale result.
This linewidth measurement is merely an estimation. The measurement is affected by several problems. The calibration of the frequency error relies on a scan of the error signal, but the unlocked laser has a free running linewidth much greater than the linewidth of the cavity an thus the slope of the error signal is broadened for any frequency scan, leading to an overestimation of the final laser linewidth. For comparison, the two different finesse measurements for the ULE indicate a broadening of the resonance by a factor of 3. Furthermore, the laser is heavily affected by acoustic noise, such that frequency jumps occur during each scan. Frequency jumps within the resonance peak render the signal completely useless, but even if they occur only in between the resonance and its sidebands, they lead to a wrong calibration of the frequency scan. Thus the laser has to be scanned much faster than it jitters. This timescale however is so short, that the oscilloscope reaches its limit resolving the full peak, making the slope shallower and thereby also leading to an overestimated final laser linewidth. Additionally, when scanning so fast ringdown effects occur in the error signal, affecting the slope of the error signal. Last but not least the error signal of the locked laser measured by the oscilloscope is also limited by the oscilloscope. These problems are why the measured linewidth of 1.6 kHz is an estimation. It indicates the order of magnitude of the linewidth, but reliable linewidth data can be achieved via the decay of Rabi oscillations when the laser light is used to excite cold atoms.
It also needs to be mentioned that laser linewidth is not the source of decoherence and a low linewidth alone does not yet guarantee long coherence times. High frequency phase noise which is above the locking bandwidth is not suppressed by the lock and furthermore, the phase noise can be amplified at high locking gain. As already mentioned, a possible way of reducing this phase noise is by filtering the light through a cavity. Also noise on the laser intensity can be problematic, as it causes fluctuations in the Rabi frequency and heating due to AC shifts during the Rydberg excitation. To reduce intensity fluctuations a separate stabilization loop is needed, which is however not being build in this thesis.

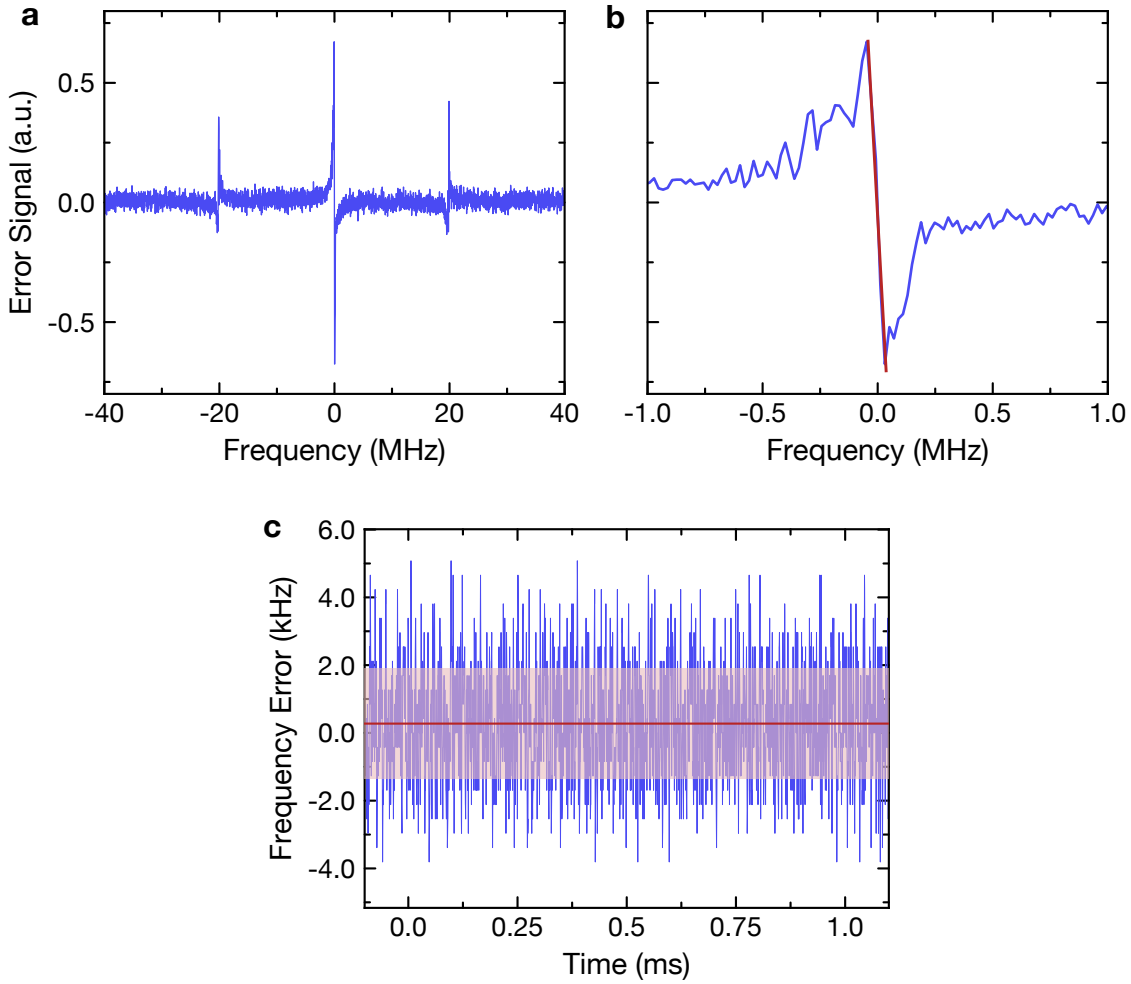

Figure 4.16 – Error Signal of the ULE Lock. Figure **a** shows the error signal of the large sideband that the laser gets locked to. The small sidebands of 20 MHz are used to determine the relative frequency of the x-axis. In **b** a zoom into the middle peak with a fit of the slope is shown. The fitted slope value is -18.9 units/MHz. This is used to determine the frequency error for the error signal of the locked laser, seen in the **c**. The red line is the mean value of the frequency and the light red area shows the standard deviation from the mean for a time of 1 ms, giving the linewidth for this time interval.

4.3 The blue 405 nm setup

In this setup coherent light of 405 nm is created via second-harmonic generation in an enhancement cavity. The frequency is stabilized to the 4S to 5P transition frequency of ^{39}K. Figure 4.17 shows a detailed schematic of the setup, including the 810 nm ECDL and its amplification as well as the doubling cavity with its lock. The frequency stabilization of the laser is not included in this schematic and is discussed separately in Section 4.3.4.
In contrast to the NIR setup, this setup is meant to output laser light at a much more challenging wavelength. Laser diodes at 405 nm have been available for almost 20 years [82],but have very limited output and hardly operate in stable single mode above a few mW of output power. This is why many setups use injection locking for these wavelengths. However injection locks are still limited to tens of mW by the diodes available, and tapered amplifiers are not operating in the blue. Since the calculations in Chapter 2 show, that several hundreds of mW are preferable in this setup, the approach taken in this project is the one of second-harmonic generation. The fundamental beam needs to have a wavelength of 810 nm, which can be amplified to 2 W just like the laser of the NIR setup. With doubling efficiencies of 30 - 40% commonly reachable, this method allows for the Rabi frequencies calculated earlier.
In the following the main building blocks of the setup are presented part by part. Their design and assembly as well as their characterization are discussed, beginning with the ECDL and the TA, followed be the doubling cavity and finally the transfer cavity, including both the laser lock to the cavity and the length stabilization.

4.3.1 The 810 nm diode laser

The laser design is the same as the Littrow laser of Section 4.2.1. The diode is a EYP-RWE-0840-06515-1500-SOT02-0000 from Eagleyard with broad gain spectrum and AR coating. The gain spectrum ranges from 790 nm to 870 nm, with a peak gain at 850 nm. The used frequency of 810 nm is thus far off the gain peak. However this is the best suitable diode Eagleyard has to offer for 810 nm. The influence of the dominant frequencies in the free running spectrum can be seen in several aspects. The calculated angle for the diffraction grating, which has a grating constant of 1800 grooves per mm, is 46.7°, but the actual set angle is below 45°, because the lower frequencies otherwise cannot be suppressed sufficiently. That means, even if the gain profile of the grating favors 810 nm, the diode will lase at about 830 nm, because these frequencies experience so much more gain. Consequently the grating has to be adjusted such, that it suppresses 830 nm even more, without completely suppressing 810 nm. This setting leads to a very high lasing threshold and to relatively unstable single mode operation.

Characterization

Figure 4.18 shows the output power of the 810 nm laser, both right after the housing and in front of the TA, when parts of the light have been split up for the lock and the

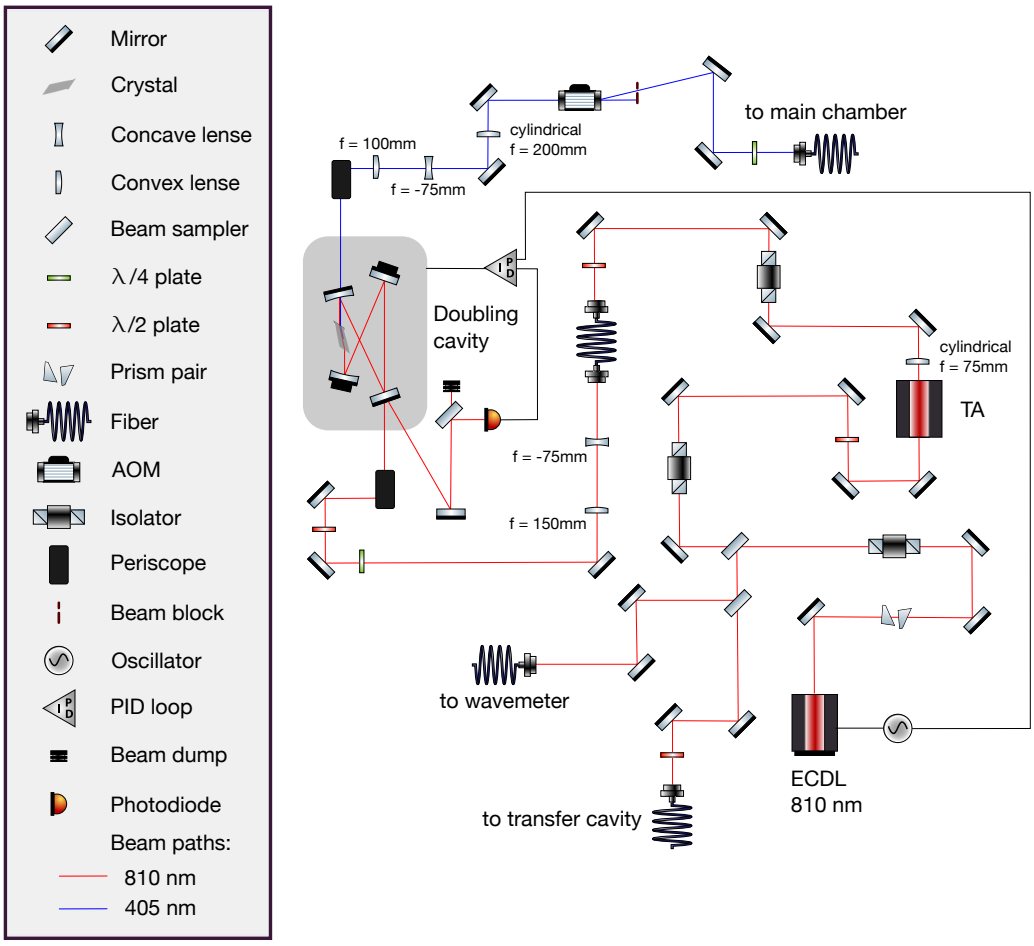

Figure 4.17 – Blue laser setup. A schematic of the blue setup is shown. The ECDL is protected by two isolators before seeding the TA. The TA output is send through a fiber and then coupled into the doubling cavity. The output is beamshaped and after an AOM coupled to a fiber that leads to the main chamber.

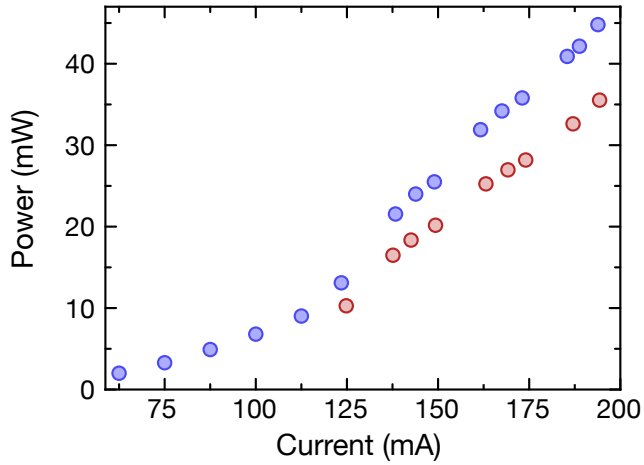

Figure 4.18 – 810 nm laser output power. The output power of the 810 nm ECDL is plotted against current. The the output right after the laser housing (blue) and the power that arrives at the TA for seeding (red) are shown. Up to about 120 mW the laser output is dominated by spontaneous emission. At 125 mW the laser operates in single mode for the currents measured in the plot.

wavemeter. The intensity at the TA is important to know for correct seeding of the TA. The measurement does not consist of equally spaced measurement points on the x-axis, but rather of several short intervals. This is because the laser only runs in single mode for certain currents, and in between the intervals of single mode behavior, the power output drops slightly, as can already be seen at the end of each measured interval. To avoid misleading information, this graph shows only the well behaved current intervals with the respective output. At about 147 mA to 150 mA the wavelength comes across the frequency of the $4S_{1/2}$ to $5P_{1/2}$ transition, which is where the laser is supposed to be stabilized. If not specified differently, this is where the laser is set for all of the following measurements.
The figure also does not show a clear lasing threshold, but rather a linear slope up to 120 mW and another linear but different slope from 120 mW on. This is because at the point of lasing there is already several mW output caused by spontaneous emission of the diode material. The spontaneous emission causes the first slope. The lasing threshold then is at about 120 mW, marking the start of the second slope. This very high lasing threshold is not due to careless alignment of the laser diode. Compared to the 980 nm laser diode, a lot of time went into the alignment of the 810 nm laser diode. It was very tricky to get it lase at this wavelength at all. This is due to the gain profile of the diode. Whenever the lasing threshold was reduced below 90 mW, the wavelength was at 820 nm or longer.
As in the NIR setup, a prism pair right after the laser is used to compensate for the elliptic output of the laser diode and an optical isolator (IOT-5-780-VLP from Thorlabs) is placed to protect the laser from back reflections. The 780 nm isolator is not perfectly suited for 810 nm, but still the best option Thorlabs offers for this wavelength. The isolation was not enough to protect the diode from the TA output, because a tapered

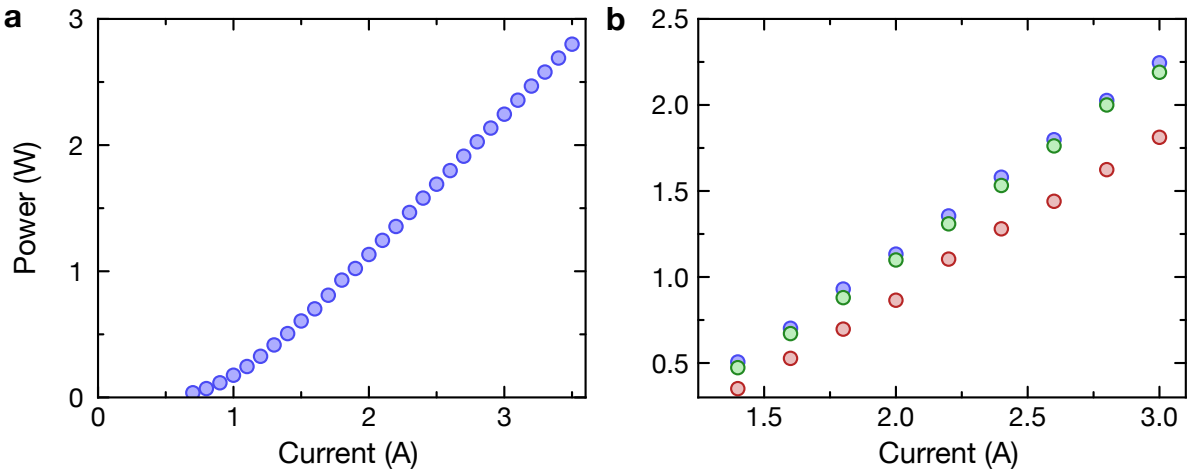

Figure 4.19 – The output power and seeding dependence of the 810 nm TA. Figure **a** shows the output power of the TA against current for 25 mW seeding. From about 1A current on the output power grows linearly. Figure **b** shows the seeding dependence on current for 25 mW seeding power (blue), 20 mW seeding (green) and 15 mW seeding (red).

amplifier always outputs some power backwards. After aligning the TA and running it at considerable power, the laser was very unstable in wavelength, such that the problem was noticed. Placing a second isolator (IO-3-780-HP from Thorlabs) right after the first one solved the problem.

4.3.2 The tapered amplifier

The amplification of the 810 nm light works with the same principle and design as discussed in the NIR setup in Section 4.2.2. The TA chip is EYP-TPA-0808-02000-4006-CMT04-0000 from Eagleyard, specified with an output power of 2 W, maximal rating 2.2 W. The center wavelength is 808 nm, with a gain width of 10 nm. So it is very well suited for 810 nm. Figure 4.19 shows the output power on current as well as the seeding dependence. With almost 3 W the output power goes well above the maximal rating of 2.2 W. This value was measured at 3.5 A current, still below the maximum rating of 4 A, which has not been measured in order to not damage the TA. The seeding dependence shows a clear increase in output when going from 15 mW to 20 mW seeding, but almost no increase between 20 mW and 25 mW seeding.

Characterization

The TA also shows a relatively strong temperature dependence, as it can be seen in Figure 4.20. The maximum output lies at about 24°C and is almost 20% higher than at 17°C. This TA does not show the oscillations in temperature that the other TA showed.

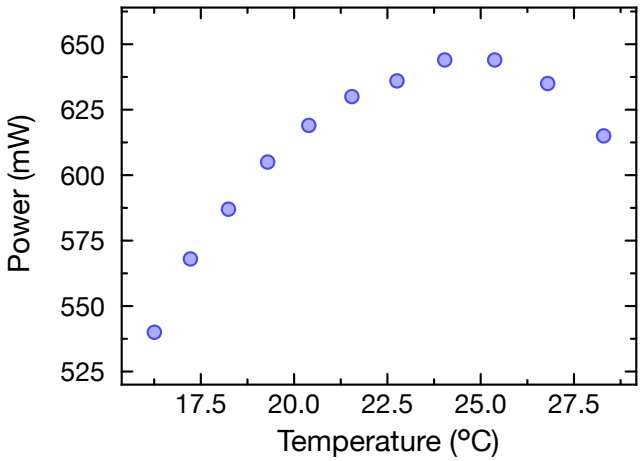

Figure 4.20 – Temperature dependence of the 810 nm TA. The plot shows the output power of the TA for different temperatures of the TA chip. The maximum lies between 24°C and 25°C.

Beamshaping and fibre coupling

As the other TA, this one has an output with different divergences for the horizontal and the vertical axis. The vertical axis is collimated using the $f = 18.4\,\text{mm}$ convex lens that is mounted in the TA housing. The horizontal axis additionally needs a cylindrical $f = 75\,\text{mm}$ lens to be collimated. Then the output still consists of a variety of different spatial modes and has a rectangular shape, but about a meter after the TA the beam profile looks more like a Gaussian. Right after the collimation lenses there are two mirrors and an isolator (IO-3-780-HP from Thorlabs), to protect the TA from back reflections. The isolator can take up to 15 W and although it is designed for 780 nm and might not be perfect for 810 nm, no problems have been observed so far. Originally the plan was to send the TA output directly towards the cavity and to couple only the Gaussian fraction in. Since the cavity itself is mode cleaning, the other modes in the input beam would not matter. However it turned out that it is very hard to properly couple the Gaussian mode when the input beam consists of several modes. One can never be sure to have reached an optimum because other modes do not disappear and the relative incoupling as it is seen on the oscilloscope depends on how the beam hits the photodiode, since different parts of the beam are made up of different spatial modes. It is also more tricky to lock the cavity when the signal has many peaks with error signals overlapping. For these reasons the beam after the TA is now coupled to a fiber and outcoupled again for the cavity. The coupling efficiency is roughly 40%, but should be improvable. The main problem is that the incoupling is very sensitive to slight changes in the coupling lens (Schäfter + Kirchhoff fiber collimator 60FC-F-4-M5-10) and adjusting the focus even a bit completely destroys the coupling. It is thus very hard to find the right focus. The beam is also not perfectly Gaussian and slightly too big yet.

4.3.3 The 810 nm to 405 nm doubling cavity

The next stage in the setup is the doubling cavity. Here the frequency doubling from 810 nm to 405 nm takes place, following the calculations given in Section 4.3.3.

Design

The doubling cavity iteself consists of 4 mirrors, purchased from Layertec and a BBO crystal from Castech. The cavity mirrors have a high reflectivity coating with $> 99.95\%$ reflectivity for 810 nm and high transmittivity of $> 99\%$ for 405 nm. The incoupling mirror is specified with $(98.8 \pm 0.1)\%$ reflectivity for 810 nm. The crystal has a Brewster cut, and dimensions of $3 \times 3 \times 10$ mm. It is heated to 80°C to prevent it from absorbing moisture. To temperature stabilize a temperature controller from Thorlabs (TC200) is used with a Omega 55016 thermistor and a resistive heater from Thorlabs (HT15W), which are both stuck into a copper mount with indium foil. The crystal is also packed into one layer of indium foil and mounted into the block. The copper block is screwed on a Vespel plate for temperature isolation and then mounted on a translation stage from Newport (9081-M).
The full design of the cavity can be seen in Figure 4.21. The translation stage with the crystal is mounted on a thick aluminum plate, which also the mirror mounts (polaris mounts from Thorlabs) can be screwed on directly. This minimizes misalignment through thermal expansion and forces acting on the plate. The plate is placed inside a thick aluminum housing with magnets, strong enough to guarantee a fixed position. The magnets are screwed on the floor of the housing and downside the aluminum plate, such that the plate can be taken out and set back on the same position on any time. This does not only allow to take the plate out, but most importantly decouples the cavity from stress in the housing. The housing has a 1 cm thick plastic lid which allows to evacuate the cavity. The forces on the housing through the evacuation will however not affect the cavity alignment because of the resonator plate. This allows for optimal stability and isolation against acoustic noise and temperature fluctuations. The design is inspired by [62].
To stabilize the length of the cavity to resonance with the laser light, two piezos are used. The slow piezo is attached to a mirror mount and has one of the curved, half inch mirrors glued on it. It can cover length fluctuations of tens of micro meters with about 1.5 kHz. In order to be faster than that, the cavity has a second, fast piezo. This piezo is only 1/4 inch in diameter and has a 1/4 inch mirror glued on it. Due to its lower mass it can react much faster than the slow piezo. To give the light piezo stability and allow expansion in direction of the mirror only, the piezo is glued on a copper mount which is filled with led. This two piezo locking is inspired by [83], where it has been shown to be a significant improvement.

Characterization of the cavity

For good incoupling, mode matching is inevitable. Without the fiber between TA and cavity, it was not possible to reliably measure the diameter of the incoming beam due

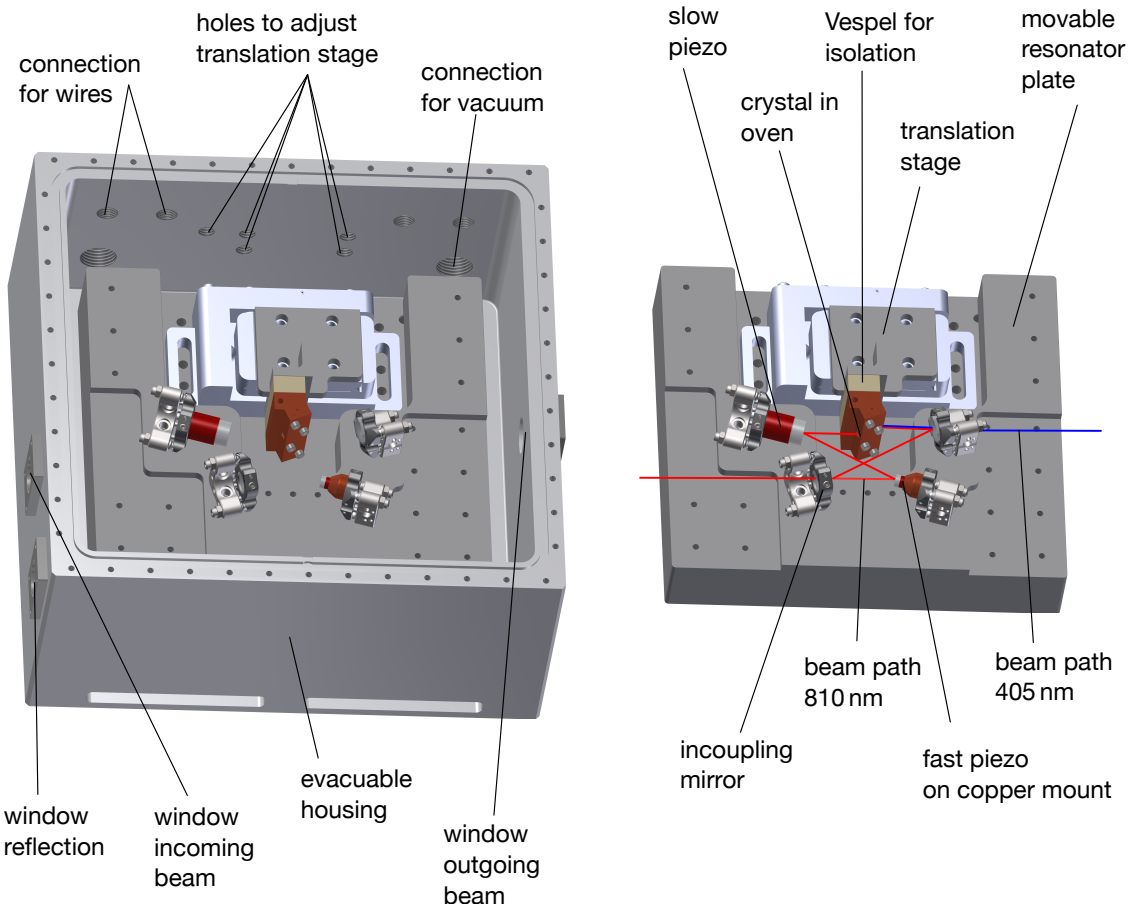

Figure 4.21 – Render of the doubling cavity. The cavity inside the housing without lid (left) is shown. The aluminum plate with crystal, mirrors and beam-path can be taken out and is shown separately (right).

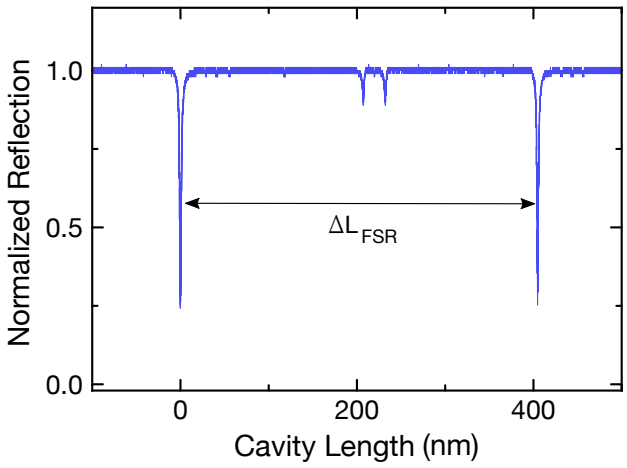

Figure 4.22 – Reflection signal of the doubling cavity. Reflection signal of the doubling cavity is plotted for a length scan with the big piezo. The two deep dips mark the resonances for the Gaussian mode. About 75% of the light is coupled into the cavity for this scan. Frequency modulation was present for this scan, but the sidebands are too small to be seen in the scan. Modulation is necessary to lock the laser since only with the laser locked is it stable enough to show these incoupling peaks.

to the overlap of several modes. After placing the fiber, the outcoupled beam has a well defined diameter and can be mode matched to the second waist of the cavity. Since space for mounting lenses on the board is very limited, a combination of lenses is used here. First a $f = -75\,\text{mm}$, followed by a $f = 150\,\text{mm}$ lens on a translation stage allow for best possible mode matching.
The incoupling itself is also much easier with the Gaussian shaped incoming beam. Without much optimization, the incoupling shown in Figure 4.22 was achieved. The figure shows the reflection signal from the cavity when the slow piezo is scanned in length and the laser is locked. Just as a frequency scan, this length scan allows to calculate the finesse of the doubling cavity as the ratio of FSR and FWHM of the Gaussian peak. For this measurement the piezo is assumed to behave roughly linear over the relevant distance. The result is a finesse of

$$\mathcal{F} = 190 \pm 50.$$

The large error is due to the uncertainty in the peak height and width, which can not be known with higher precision from the obtained data. This finesse measurement is not determined by the mirrors only, but is largely affected by the crystal. A measurement of the finesse without crystal is not possible since the Brewster cut is crucial for the beam path. This means that reflection on the Brewster cut, absorption in the crystal and second-harmonic generation contribute to the losses in the cavity. This affects the incoupling and thereby the finesse of the cavity.

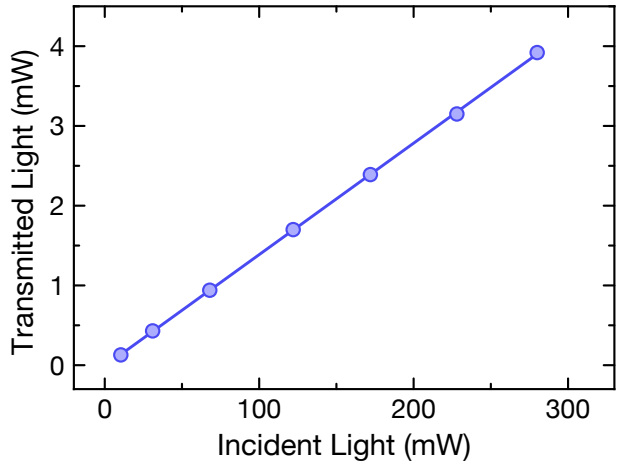

Figure 4.23 – Transmission of the incoupling mirror. The blue dots show the transmitted versus incident light for the incoupling mirror of the doubling cavity. The blue line is a linear fit, giving a transmission of $T = 1.40 \pm 0.05\%$.

Figure 4.23 shows a measurement of the incoupling mirror. The transmission through the first mirror into the cavity was measured for different powers of the incoming beam. The transmission was measured to be $T = 1.40 \pm 0.05\%$. Assuming there is no reflection on the AR coated side as well as no losses, the reflectivity is

$$R_{\text{in}} = 98.60 \pm 0.05\%,$$

which is 0.1% less than the lowest value within the error bars specified by the supplier. Assuming there are further losses, the reflectivity is even lower.

Characterization of the lock

To stabilize the length of the cavity to resonance with the 810 nm light, a PDH lock is used. The reflection from the cavity is send to a photodiode and the obtained signal is used to stabilize the length to the resonance. The laser itself is modulated in current in order to generate the necessary sidebands. The protection board used in the laser as cited in Section 4.2.1, has a branch for AC current modulation. To account for the polarity of the laser diode the protection board had to be extended. Current modulation for this diode only works if the anode and cathode branches of the original design are swapped. The current is modulated at 15 MHz, which is relatively slow for the cavity, but the transformer of the protection board does not allow for faster modulation. The frequency sidebands get amplified by the TA and pass through the fiber before getting to the cavity.
Figure 4.24 shows the error signal of the cavity when it is scanned and when it is locked. The scanned signal shows the three zero crossings typical for a PDH signal, but compared to the other PDH signals in this thesis, the signal stays at high value in between the sidebands and the main peak. This is because the modulation frequency

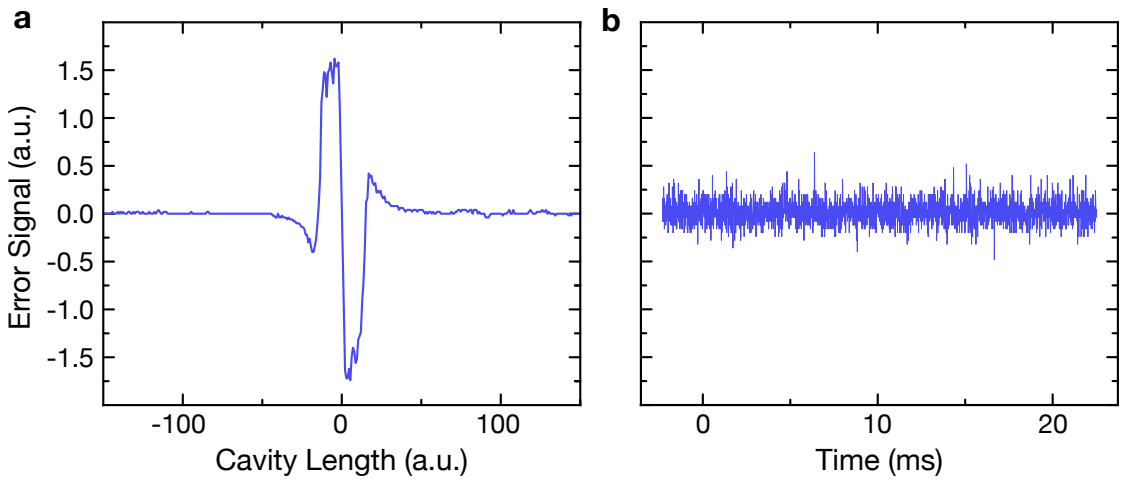

Figure 4.24 – Error signal of the SHG cavity lock. The left plot shows the error signal of the doubling cavity when the cavity is scanned in length. It shows the three zero crossings of a PDH signal, where the middle crossing corresponds to the Gaussian mode and the ones on the sides are given by the sidebands. The features of the sidebands can not be fully resolved from the main peak because they are too close to the main peak. The plot on the right shows the error signal for the cavity locked to the main peak.

of 15 MHz is comparable to the width of a resonance peak in the cavity, such that the sidebands cannot be resolved properly. This lack of resolution is not problematic, because the central zero crossing can still be used to lock the cavity. The error signal for the locked cavity shows that the lock stays well below the maximum of the scanned error signal.
The possibility to lock the cavity also crucially improved when the TA output was coupled to a fiber first. Before placing the fiber, the many spacial modes that where coupled to the cavity resulted in the error signals of different peaks interfering with each other. Many zero crossing were so close to each other, that it was not possible to stabily lock the cavity.

Characterization of the second-harmonic generation

BBO crystals have an extremely low acceptance angle, which is why it is very hard to align it to the right phase matching angle. That means the alignment procedure is very lengthly, because even if the cavity is aligned very well to the Gaussian mode, it might not allow for proper phase matching. Only if the beam lies exactly in the cavity plane do the curved mirrors lead to the correct waist in the crystal and only if the angle between beam and crystal is right, will it be phase matched. The crystal position can be adjusted, but if the beam has the wrong angle, adjusting the crystal to phase matching does not allow to keep the round trips aligned to each other. This means the procedure of aligning the cavity consists of consecutive alignments of the crystal, the round trip, and the incoupling.

The main limitation which has prevented good alignment so far, are the incoupling mirrors. Because of the periscope the last mirror is about 20 cm away from the incoupling mirror and because of the limited space the second last mirror is only 5 cm further away. This is a bad constellation for alignment. Additionally the mirror mounts (SR050-050L-2 from Liop-Tec) can be tricky in alignment. While it does not matter for the rest of the setup, for the doubling cavity the effects are quite visible. The mirrors often do not fall back to the same position if moving the alignment screws back and forth. With the cavity so far from the mirrors and so sensitive to alignment, the signal randomly jumps when adjusting the mirror and the change cannot be reversed. This makes the alignment even more time consuming than it already is.
Another problem seems to be that the mirrors need to be cleaned regularly, noticeable by a significantly increased output power after the cleaning. The most likely reason for this is outgasing from the resistive heater used to temperature stabilize the crystal. The crystal is the element which is closest to the resistive heater and is thus probably most contaminated from the outgasing. Since the crystal mount has a straight 90° surface, whereas the crystal has a Brewster cut, it is not possible to reach the crystal surface while the crystal is inside the mount. This means that the crystal cannot be cleaned and the light passes through the dirty crystal surface in every roundtrip.
At this point the maximum measured output of the second harmonic was 7 mW with an incoming power of 400 mW. With 75% incoupling this means that about 300 mW were coupled in to the cavity. This low power is due to the bad coupling efficiency of the fiber coupling of the TA. For the output one has to add the fraction of the power that has been reflected on the Brewster surface. This is 21.8% of the blue light and thus 8.5 mW blue light were produced in the cavity. This corresponds to a conversion efficiency of a bit more than 2.8%. The expected conversion efficiency for this power for perfect alignment according to the calculations would be 18% efficiency. The cavity thus still needs quite some optimization.

Beamshaping

The beamprofile after the SHG is quite elliptic because of the large walk-off of BBO. Thus some beamshaping is necessary. Due to the different waist sizes in the sagittal and tangential plane, the two axes also diverge differently. The best beamprofile of the output beam has been achieved for an $f = 100\,\text{mm}$ convex lens right after the periscope, followed by a $f = -75\,\text{mm}$ concave lens, which already collimates one axis. To collimate also the second axis, a cylindrical lens of $f = 200\,\text{mm}$ is used.
The AOM and fiber coupling are not yet aligned, because changes in the doubling cavity still have to be made, which changes the alignment afterwards.

4.3.4 Locking to the transfer cavity

To stabilize the 810 nm laser there are several possibilities. First of all one has to decide whether to use the 810 nm light, or the 405 nm light for stabilization. An advantage of the 405 nm light would be the possibility of a spectroscopy lock to the 4S to 5P transition. The laser is then automatically locked to the transition without any long term

drifts occurring. A downside of a lock to the transition in this setup is the large detuning of several GHz needed for the single atom gates, as calculated in Section 2.3. Probably several passes through more than one AOM would be needed to achieve this detuning, such that the availability of the transition is not very useful. Using the 810 nm light for the stabilization on the other hand has the advantage of having the locking decoupled from the doubling. The PID loop of the frequency stabilization only relies on the laser itself and the elements used in the lock. The 405 nm light gets influenced by fluctuations in the length stabilization of the doubling cavity, fluctuations in the crystal temperature, and other fluctuations in the doubling efficiency, as well as fluctuations in the amplification of the 810 nm light. It is much more favorable to decouple these fluctuations from the laser lock to avoid unwanted loops.
For these reasons a small fraction of the 810 nm light is split off and used for locking. A cavity lock allows for arbitrarily high detunings and additionally lower linewidths than the spectroscopy lock. As already mentioned in Section 4.2.3, one wants low thermal expansion of the cavity to ensure long term stability. Unfortunately the ULE cavity used for the IR setup, is not coated for the 810 nm light. Instead another cavity is used, which is not very stable regarding temperature fluctuations. The idea is to lock the 810 nm laser to this cavity, which assures short term stabilization of the laser. To assure long term stabilization the cavity is stabilized to another laser, which is itself stabilized to the ULE. This is possible because there is a piezo in the cavity to change adjust the length and because both the ULE as well as the other cavity are coated for 770 nm, allowing to use the 770 nm laser to stabilize the cavity to the ULE. The cavity is thus called a *transfer cavity*. Figure 4.25 shows the setup for the transfer cavity. The whole setup is additionally protected by a wooden box.

Transfer cavity

The cavity consists of two curved mirrors with a curvature of 50 cm, located inside a thick brass tube. They have a high reflectivity coating from 770 nm to 810 nm from Advanced Thin Films. One mirror is screwed inside the tube while the other is glued on a piezo. The piezo is also inside the brass tube, being fixed on a backplate which is screwed on the tube. The tube is placed inside a vacuum chamber for isolation from the environment. The cavity is not actively temperature stabilized, but only isolated through the vacuum. The piezo and the brass tube are not stable in length and can drift by several GHz per day due to the lack of temperature stabilization. The advantage of the piezo is the possibility of active length stabilization with respect to a reference. In this case the ULE cavity is used as a stable reference via a 770 nm laser because it matches the coatings of both cavities. The linewidth of the locked 770 nm laser is much smaller than its peak width on the transfer cavity and thus does not have a considerable effect on the quality of the transfer lock.

Cavity characterization for 810 nm

The 810 nm is locked to the transfer cavity using a PDH lock. The sidebands are generated by current modulation of the laser at 15 MHz, as already discussed for the lock

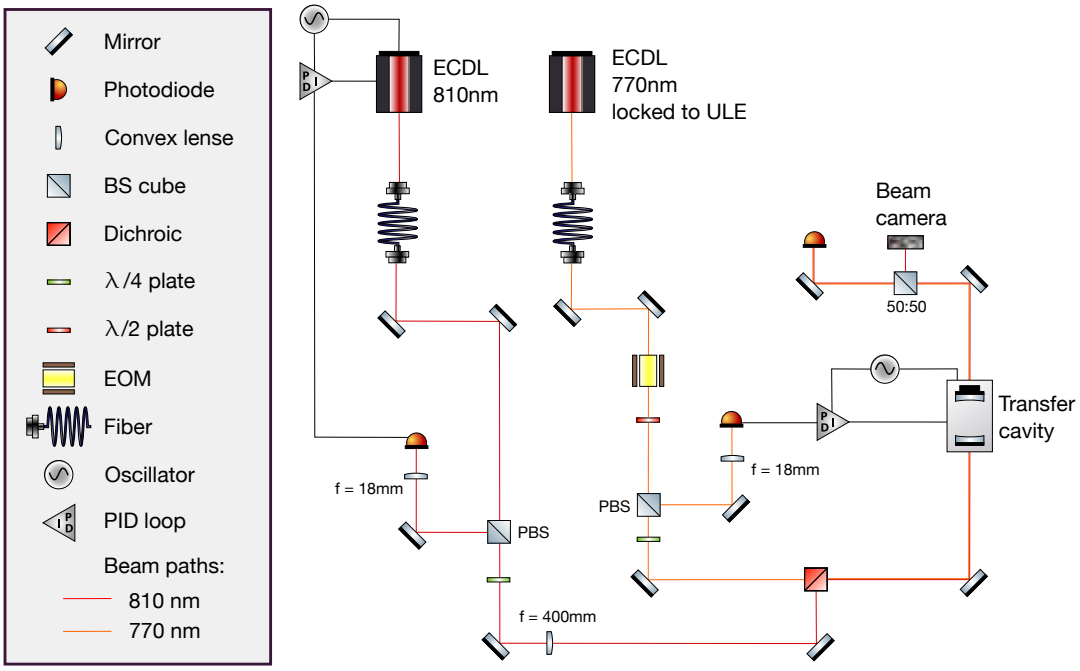

Figure 4.25 – Transfer cavity setup. The figure shows the detailed setup for the transfer cavity. Both laser enter the cavity from the same side. While the 810 nm is modulated in current, the 770 nm gets sidebands by an EOM.

of the doubling cavity in 4.3.3. In contrast to the 980 nm laser, this lock does not need large and small sidebands. As seen from the detuning calculations in Chapter 2, the detuning should be several GHz large and a displacement of hundreds of MHz from the optimum does not have a severe effect. The roughly 1 GHz FSR and the possibility to lock the 770 nm on different modes gives enough freedom to adjust the detuning. About 200 µW are coupled out of the fiber for the lock. Scanning the cavity length or laser frequency shows that the laser is very vulnerable to acoustic noise. The signal height varies by 70% and drifts in the diode cause mode jumps and power fluctuations. This is because of the problematic diode, as it has already been discussed.
Figure 4.26 shows the transmission signal of the 810 nm laser on the transfer cavity when the frequency of the laser is scanned. The scan shows the FSR with two subsequent peaks of Gaussian modes. In between the main peaks two other modes can be seen that also get coupled to the cavity. The laser is modulated in current for this scan, but the 15 MHz sidebands are too small to be seen on the scan. What is remarkable on this scan is the large offset of the background of about 20% of the main signal. This is not due to an offset of the photodiode or the oscilloscope and has been plotted with proper calibration of the zero level. This background is actually there in the light, shining through the cavity. A camera in the transmission beam shows constant saturation at any frequency of the laser. This is a continuous sea of frequencies, probably due to spontaneous emission of the diode. The stimulated emission is not dominant enough to completely suppress other frequencies. The background disappears when placing a (810 ± 10) nm filter in front of the photodiode, proving that there is in fact

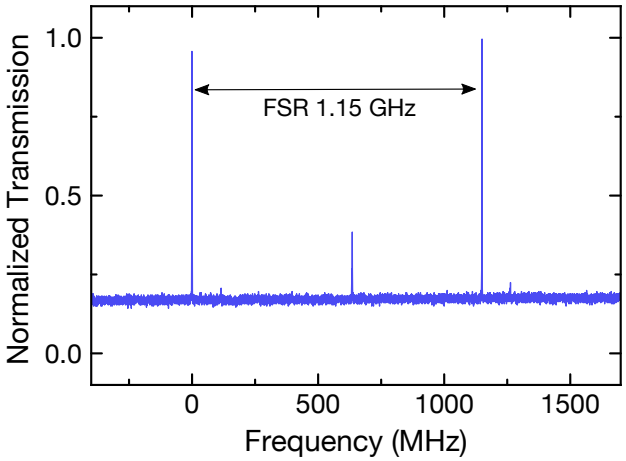

Figure 4.26 – 810 nm transmission through the transfer cavity. The plot shows the transmission signal of the 810 nm laser through the transfer cavity. The two Gaussian modes are separated by a free spectral range of approximately 1.15 GHz. The laser is modulated in current with 15 MHz, but the generated sidebands are too small to be seen on the scan.

other frequencies in the laser beam. Except for an offset both in the transmission and the reflection signal, this does however not have much of an effect for the lock.

The transmission signal cannot be used to calculate the finesse because of its strong jittering. Instead, as for the ULE, the ringdown in the reflection signal is used to measure the finesse. For that the laser has to be scanned very fast, more than twice as fast as for the ULE ringdown. Only then can a continuous oscillating signal without effects of jittering be measured. Figure 4.27 shows this ringdown signal and a fit of the theoretical curve to the data. The fitted ringdown time is $\tau = 1.37 \pm 0.02\,\mu s$, which corresponds to a finesse of

$$\mathcal{F} = 10\,000 \pm 200.$$

As it can be seen in the plot, this measurement is not very reliable. Especially the first few peaks are not well matched with the fit. The error of 2% given by the fit also takes into account that the theoretical curve fits the data very well for later values and is thus relatively small, but taking into account that the scan was very fast and that the oscilloscope is reaching its limits to resolve this, one can expect that the first peaks are most likely too small in the data. Also the instability of the laser might have led to problems while taking the data, such the the taken data is not representative for the ringdown in the first place. The finesse is thus most likely overestimated in this measurement and the error only corresponds to the error of the fit to the data, but is not representative for the error of the plotted data regarding the actual ringdown.

For locking the same electronics as for the ULE is used, namely a slow piezo and a Toptica FALC 110 for the fast current feedback. Figure 4.28 shows the error signal of the 810 nm laser on the transfer cavity both for the locked and scanned case. For the scanned case the error signal is clearly disturbed by the instability of the laser. A

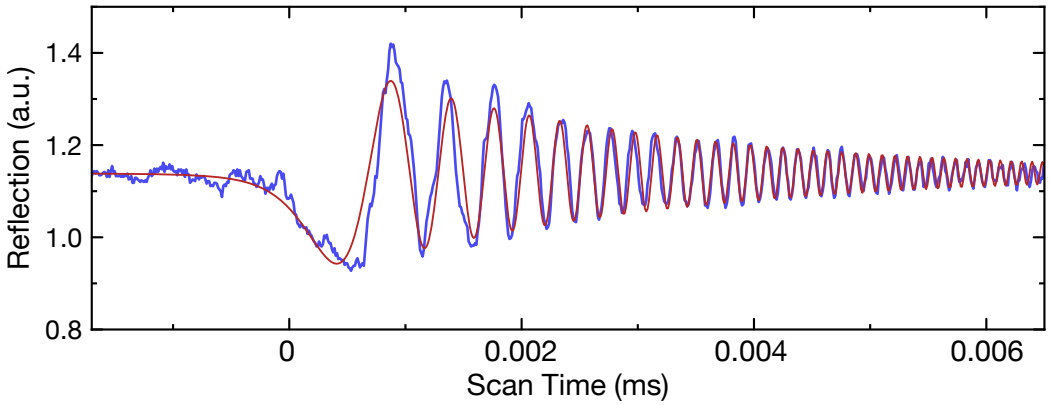

Figure 4.27 – Transfer cavity ringdown in the 810 nm reflection signal. The plot shows the reflection signal for a fast scan over the resonance (blue).The ringdown oscillations can be seen clearly over about 5 µs. The red curve is a fit of the theoretical ringdown curve to the data, giving a ringdown time of $\tau = 1.37 \pm 0.02\,\mu s$. The theoretical curve does not fit the data very well. The theoretical curve decays slower than the measured curve, indicating an overestimation of the ringdown time.

zoom into the slope of the main peak shows that even clearer. Instead of one slope, several wiggles are seen. It took several shots to get this one, where the main slope can be clearly identified. Increasing the scan rate would lead to a less disturbed measurement, but this is the maximal speed at which the error signal still roughly shows its real height. For all faster scans the error signal is too much affected by the resolution of the oscilloscope.
The linear fit in the zoomed slope allows to assign a frequency error to each height of the error signal. With this a frequency error can be assigned to each point in the measured error signal for the locked laser. In the figure of the locked signal the frequency error has been plotted against time. The standard deviation from the mean is

$$\Delta\nu = 37\,\text{kHz}.$$

This is only an estimation. The error signal scan measured with the oscilloscope is not a reliable source for the slope of the error signal. Nevertheless it hints at a linewidth more than 20 times bigger than for the 980 nm laser.

4.3.5 Stabilizing the transfer cavity

To stabilize the transfer cavity, a 770 nm laser is used, which is itself stabilized to the ULE cavity. The laser is home-built as well, but with a linear design [84] instead of the Littrow design. It is used as a Raman laser in the context of the experiment and has been built in the course of a bachelor's thesis [74]. Since an identical laser has been built at the beginning of this master project, but with an MTS [85], instead of a ULE lock, the design and behavior of these linear lasers compared to the Littrow lasers is

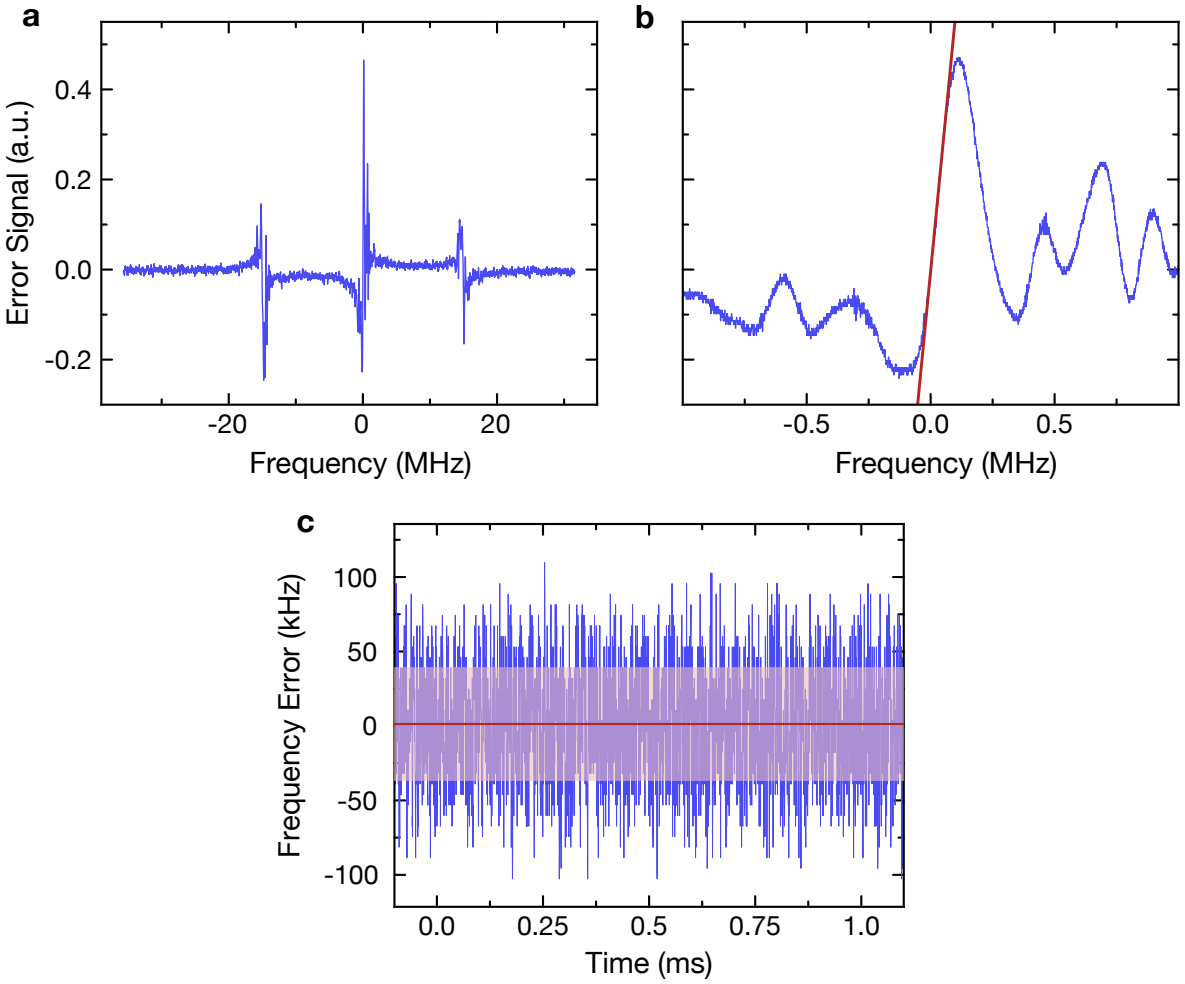

Figure 4.28 – 810 nm error signal of the transfer cavity lock. Figure **a** shows the error signal for a frequency scan of the 810 nm laser. The sidebands are used to set the frequency of the x axis. In **b** a zoom into the middle peak with a fit of the slope is shown. The fitted slope value is 5.65 units/MHz. This is used to determine the frequency error for the error signal of the locked laser, seen in the **c**. The red line is the mean value of the frequency and the light red area shows the standard deviation from the mean for a time of 1 ms, giving the linewidth for this time interval.

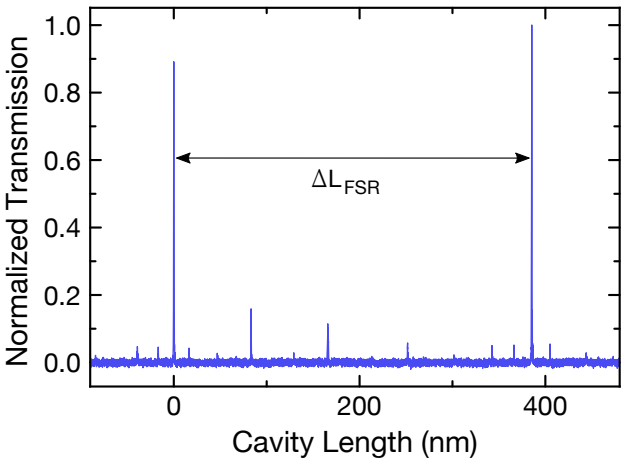

Figure 4.29 – 770 nm transmission through the transfer cavity. The plot shows the transmission of the 770 nm laser for a length scan of the cavity. The laser is locked to the ULE and the light is phase modulated via an EOM for this measurement. The 55 MHz sidebands can bee seen right next to the main peaks.

shortly discussed in Appendix B. The lock of the linear to the ULE was not part of this project and is therefor not discussed.
The cavity is locked to the laser with a PDH lock. About 120 µW are coupled out of the fiber for the lock. The sidebands are created using a home-built EOM consisting of a LiNbO3 crystal mounted between two capacitor plates, which are in row with an inductor. The resonance frequency of such an LC circuit is given by $\omega_0 = 1/\sqrt{LC}$. In this case it is measured to be 54.03 MHz, which corresponds to the frequency of the sidebands caused by the EOM. Figure 4.29 shows a length scan of the cavity. Two subsequent resonance peaks of the Gaussian mode can be seen, as well as their sidebands and some other modes that are coupled in slightly. The scanned length between the two peaks is determined by the wavelength of the light to be $\Delta L = \lambda/2$, whereas the scanned length between the main peak and the sidebands depends also on the length of the cavity. it is given by

$$\delta L = \frac{1}{2} n \, \delta\lambda = \frac{1}{2} \frac{2L}{\lambda_{\text{laser}}} (\lambda_{\text{laser}} - \lambda_{\text{sidebands}}).$$

This length distance can be obtained from the plot to be $\delta L = 18.05 \pm 1.5$ nm. This allows to calculate the length of the cavity and thus the free spectral range. The length of the cavity is unknown because the mirrors were screwed in the brass tube without keeping notice of the length. The cavity length extracted from the plot is

$$L = 13 \pm 1 \, \text{cm},$$

where the uncertainty is due to the nonlinearity of the piezo, estimated by the deviation of the leftmost sideband from the rightmost sideband in the scan. The finesse

measured for the 770 nm light is

$$\mathcal{F} = 3000 \pm 100,$$

also measured from the cavity scan. For this wavelength no ringdown was fitted, because this laser allows with high precision to measure the width of the resonance peak. The uncertainty only arises due to the nonlinearity of the piezo.

Figure 4.30 shows the error signal of the transfer cavity both for a scan of the cavity length and for the cavity locked to the laser light. The scanning length of the cavity is known through the sidebands. A linear fit to the slope of the error signal allows to assign a length error to the signal height for the locked error signal. Calculating the standard deviation from the mean over a time of 1 ms leads to a length locking of

$$\Delta L_{\text{lock}} = 3\,\text{pm}.$$

For the 810 nm a change of 3 pm corresponds to a frequency change of 9 kHz. This is below the linewidth of the 810 nm laser by about a factor of 4. It is thus not limiting the laser linewidth, but does give a minor, non-negligible contribution.

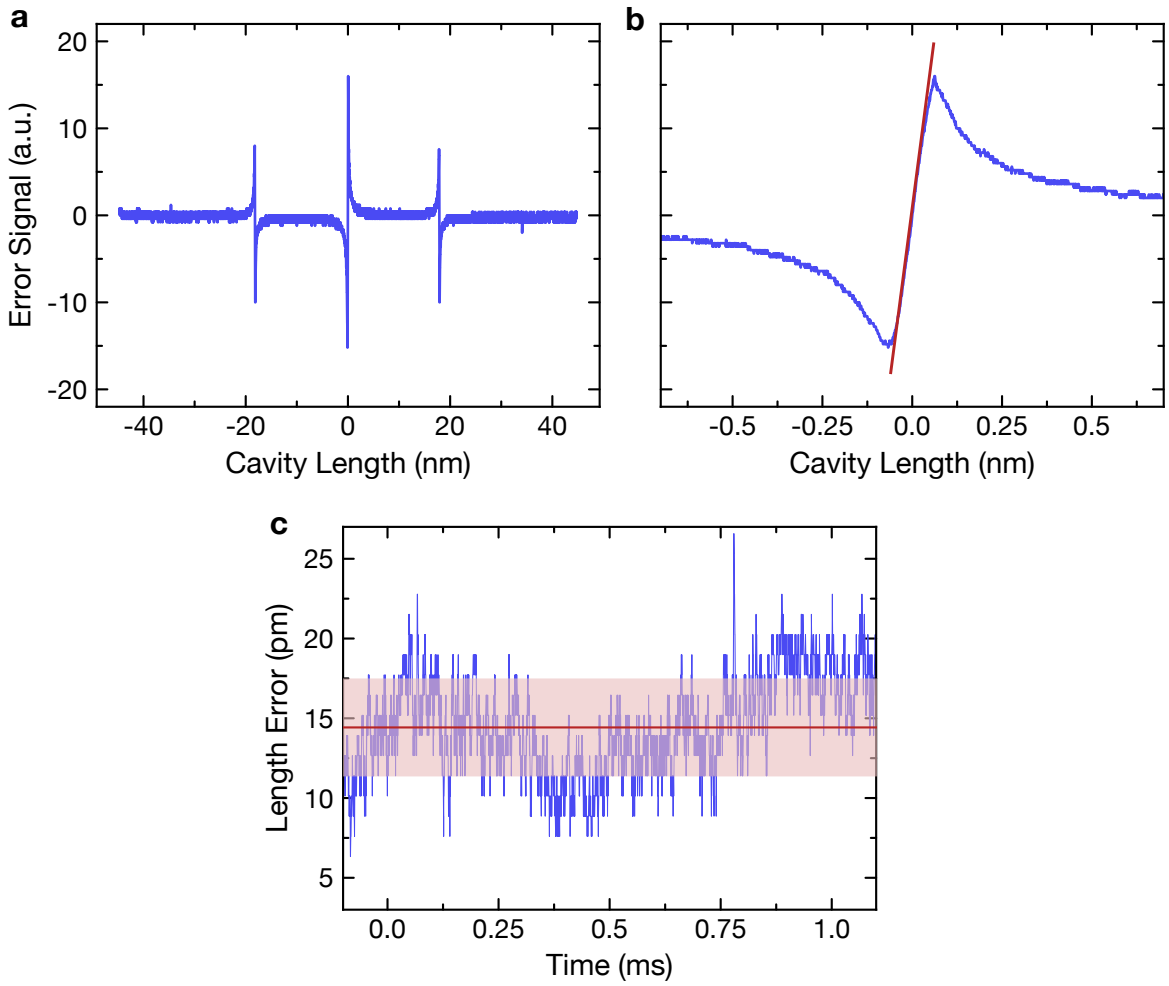

Figure 4.30 – Error signal of the transfer cavity. Figure **a** shows the error signal for a length scan of the cavity when the 770 nm laser is locked on the ULE. The sidebands are used to set the length of the x axis. In **b** a zoom into the middle peak with a fit of the slope is shown. This is used to determine the length error for the error signal of the locked laser, seen in the **c**. The red line is the mean value of the length error and the light red area shows the standard deviation from the mean for a time of 1 ms.

CHAPTER 5

Conclusion and outlook

5.1 Conclusion

This thesis has reported on the planning, construction and characterization of a laser setup for two-photon Rydberg excitation of ^{39}K. First the theoretical background of two-photon Rydberg excitation and the level structure of potassium has been introduced. These have been used to estimate Rabi frequencies and detunings for the planned setup. The calculations revealed that the limitations of the setup regarding coherence time and Rabi frequency can be pushed by a doubling cavity to increase the achievable power as well as a cavity for frequency stabilization to reduce linewidth and allow for arbitrary detuning. Consequently, the theory of frequency doubling was introduced and the geometry for the doubling cavity was calculated.
The two setups corresponding to the two transitions of the Rydberg excitation where then discussed, including the design, schematics of the different parts and their characterization. With the setup for the 5P to 50S transition more than 500 mW of infrared light were obtained. Frequency stabilization to a ULE cavity lead to a linewidth of 1.6kHz. It was shown that the laser can be locked to any frequency independent of the cavity resonances through the use of two pairs of sidebands. For the setup for the 4S to 5P an infrared laser setup was constructed and stabilized to a transfer cavity with a linewidth measured to be 37 kHz. The frequency doubling in an enhancement cavity was shown to output light at the desired frequency of 405 nm, while the cavity could be stabilized in length. The alignment of the doubling cavity profited a lot from including a fiber in between the amplification and the cavity, but still suffers from the large distance between cavity and mirrors and the sensitivity of the mirror mounts. It was pointed out that both setups suffer from instabilities in the lasers and their sensitivity to acoustic noise, where doubled laser is much more critical. The reasons given were the particular design of the external cavity diode laser and the unfavorable gain profile of the diode.

5.2 Outlook

The main application of the setup to excite Rydberg atoms in the vacuum chamber of the experiment. A first observation can be to detect Rydberg states by ionization. Furthermore EIT spectroscopy is possible, where a transmission peak is observed when both laser are exactly on resonance. Afterwards the single site addressing of the NIR laser can be set up and used to perform single-atom gates in an optical tweezer. Additionally to the Rydberg excitation, the blue light of this setup could be used for a magneto-optical trap (MOT). A MOT uses scattering on an excited state to cool the atoms. The 4S to 5P transition is narrower than the 4S to 4P transition which is used for the current MOT and would thus lead to lower temperatures. This application needs a smaller detuning than the two-photon excitation, such that a fiber EOM as in the NIR setup might be necessary to determine the detuning via a second pair of sidebands.
Future plans on the laser system are the optimization of the cavity and rearrangement of the setup. Placing the cavity on the main table will avoid a fiber after the cavity a thus reduce losses. Furthermore the periscope could be spared by using higher one-inch mirrors, reducing both sensitivity to mirror imperfections and the distance to the cavity. Further improvements will be done concerning the lasers. The Littrow lasers will be changed from the current design to a linear laser design as discussed in Appendix B, because of the observed stability of the linear lasers. The reduced sensitivity to acoustic noise as compared to the Littrow lasers and the integrated filtering of unwanted frequencies increase stability especially for the 810 nm laser and will allow for easier handling and smaller linewidths of the lasers. One could furthermore place filter cavities optimized for high transmission in the beam path to reduce phase noise and intensity stabilize the light before it is send to the atoms.

APPENDIX A

Circuit for sideband generation

To generate the sidebands for the ULE lock, two modulation frequencies have to be combined. Figure A.1 shows the circuit. The large sidebands are generated by the DDS and a doubler, because the DDS can only give up to 400 MHz. The small sidebands are generated by a function generator. The frequency doubler needs above 1 dBm, whereas the DDS can give up to 0 dBm. Thus an amplifier is used. The combined frequencies are amplified after the combiner in order to not damage the combiner with too much power.

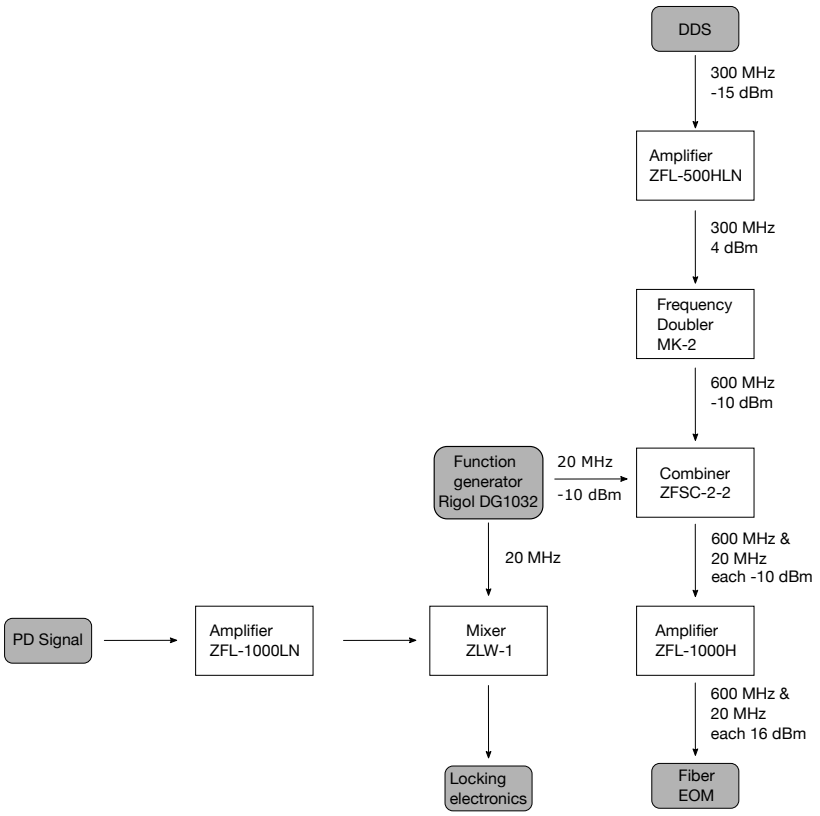

Figure A.1 – Sideband generating circuit. The circuit generating the combined large and small modulation frequencies for the ULE lock is shown. The white components are from minicircuits, whereas the diverse other components are marked in gray.

APPENDIX B

Linear laser vs. Littrow laser

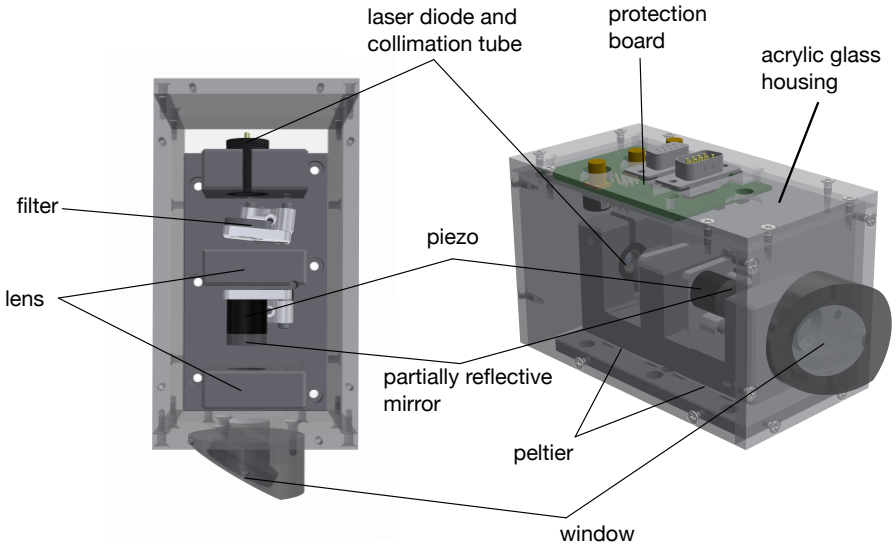

Figure B.1 – Render of the linear laser. The lenses and the diode are fixed in the aluminum mounts, whereas the piezo and filter holders are fixed with screws. Both piezo and filter can be adjusted in angle using three adjustment screws each.

Figure B.1 shows the design of the linear lasers, as they are used for the length stabilization of the transfer cavity in Section 4.3.5. The design is inspired by [84]. Next to the diode in the collimation tube is the filter. Depending on the filter angle only a small frequency range can pass. After the filter is a lens, focusing the light on the cavity mirror. The mirror is fixed on piezo, such that the cavity length can be scanned. The mirror has 30% reflection for 770 nm. The last element is a second lens to collimate the beam again after the mirror. All elements are fixed central on the beam line, making it much more robust than the Littrow laser design.
Figure B.2 shows a comparison of the 770 nm linear laser with the 980 nm Littrow laser. Both laser were scanned in frequency with the same speed and the transmission through the ULE cavity was measured. The linear laser shows one well defined transmission peak with relatively smooth slope. The Littrow laser on the other hand does not show one, but many peaks. This is because of the heavy jittering of the laser. The 980 nm Littrow laser used for this data still behaves much better than the 810 nm

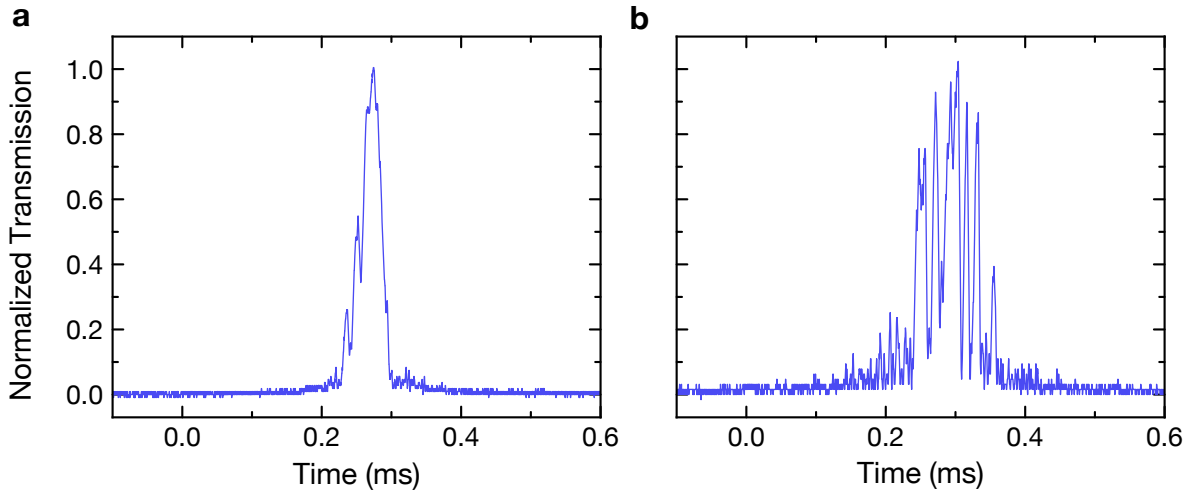

Figure B.2 – Comparison linear laser and Littrow laser. Figure **a** shows the transmission through the ULE for a frequency scan of the 770 nm linear laser. The scanning speed is 2.7 MHz per second. Figure **b** shows the transmission through the ULE for a frequency scan of the 980 nm Littrow laser. The scanning speed is 2.6 MHz per second

Littrow laser and was set to the wavelength where it showed best performance. Nevertheless the 980 nm Littrow laser is much less stable than the linear laser, making it also harder to handle and lock it.

Bibliography

1. Anderson, M. H., Ensher, J. R., Matthews, M. R., Wieman, C. E. & Cornell, E. A. Observation of Bose-Einstein Condensation in a Dilute Atomic Vapor. *Science* **269,** 198–201 (1995) (cit. on p. 1).
2. Davis, K. B. *et al.* Bose-Einstein Condensation in a Gas of Sodium Atoms. *Phys. Rev. Lett.* **75,** 3969–3973 (1995) (cit. on p. 1).
3. DeMarco, B. & Jin, D. S. Onset of Fermi Degeneracy in a Trapped Atomic Gas. *Science* **285,** 1703–1706 (1999) (cit. on p. 1).
4. Bloch, I., Dalibard, J. & Zwerger, W. Many-body physics with ultracold gases. *Rev. Mod. Phys.* **80,** 885–964 (2008) (cit. on p. 1).
5. Eisert, J., Friesdorf, M. & Gogolin, C. Quantum many-body systems out of equilibrium. *Nature Physics* **11,** 124 (2015) (cit. on p. 1).
6. Bloch, I., Dalibard, J. & Nascimbène, S. Quantum simulations with ultracold quantum gases. *Nature Physics,* 267 (2012) (cit. on p. 1).
7. Georgescu, I. M., Ashhab, S. & Nori, F. Quantum simulation. *Rev. Mod. Phys.* **86,** 153–185 (2014) (cit. on p. 1).
8. Bloch, I. Ultracold quantum gases in optical lattices. *Nature Physics* **1,** 23 (2005) (cit. on p. 1).
9. Greiner, M., Mandel, O., Esslinger, T., Hänsch, T. W. & Bloch, I. Quantum phase transition from a superfluid to a Mott insulator in a gas of ultracold atoms. *Nature* **415,** 39 (2002) (cit. on p. 1).
10. Jördens, R., Strohmaier, N., Günter, K., Moritz, H. & Esslinger, T. A Mott insulator of fermionic atoms in an optical lattice. *Nature* **455,** 204 (2008) (cit. on p. 1).
11. Schneider, U. *et al.* Metallic and Insulating Phases of Repulsively Interacting Fermions in a 3D Optical Lattice. *Science* **322,** 1520–1525 (2008) (cit. on p. 1).
12. Bakr, W. S., Gillen, J. I., Peng, A., Fölling, S. & Greiner, M. A quantum gas microscope for detecting single atoms in a Hubbard-regime optical lattice. *Nature* **462,** 74 (2009) (cit. on p. 1).
13. Sherson, J. F. *et al.* Single-atom-resolved fluorescence imaging of an atomic Mott insulator. *Nature* **467,** 68 (2010) (cit. on p. 1).
14. Parsons, M. F. *et al.* Site-Resolved Imaging of Fermionic ^{6}Li in an Optical Lattice. *Phys. Rev. Lett.* **114,** 213002 (2015) (cit. on p. 1).
15. Omran, A. *et al.* Microscopic Observation of Pauli Blocking in Degenerate Fermionic Lattice Gases. *Phys. Rev. Lett.* **115,** 263001 (2015) (cit. on p. 1).

16. Haller, E. *et al.* Single-atom imaging of fermions in a quantum-gas microscope. *Nature Physics* **11,** 738 (2015) (cit. on p. 1).

17. Cheuk, L. W. *et al.* Quantum-Gas Microscope for Fermionic Atoms. *Phys. Rev. Lett.* **114,** 193001 (2015) (cit. on p. 1).

18. Cinti, F. *et al.* Supersolid Droplet Crystal in a Dipole-Blockaded Gas. *Phys. Rev. Lett.* **105,** 135301 (2010) (cit. on p. 1).

19. Dalla Torre, E. G., Berg, E. & Altman, E. Hidden Order in 1D Bose Insulators. *Phys. Rev. Lett.* **97,** 260401 (2006) (cit. on p. 1).

20. Micheli, A., Brennen, G. K. & Zoller, P. A toolbox for lattice-spin models with polar molecules. *Nature Physics* **2,** 341 (2006) (cit. on p. 1).

21. Baier, S. *et al.* Extended Bose-Hubbard models with ultracold magnetic atoms. *Science* **352,** 201–205 (2016) (cit. on p. 1).

22. Mattioli, M., Dalmonte, M., Lechner, W. & Pupillo, G. Cluster Luttinger Liquids of Rydberg-Dressed Atoms in Optical Lattices. *Phys. Rev. Lett.* **111,** 165302 (2013) (cit. on p. 1).

23. Lu, M., Burdick, N. Q., Youn, S. H. & Lev, B. L. Strongly Dipolar Bose-Einstein Condensate of Dysprosium. *Phys. Rev. Lett.* **107,** 190401 (2011) (cit. on p. 1).

24. Yan, B. *et al.* Observation of dipolar spin-exchange interactions with lattice-confined polar molecules. *Nature* **501,** 521 (2013) (cit. on p. 1).

25. Weimer, H., Müller, M., Lesanovsky, I., Zoller, P. & Büchler, H. P. A Rydberg quantum simulator. *Nature Physics* **6,** 382 (2010) (cit. on p. 1).

26. Saffman, M., Walker, T. G. & Mølmer, K. Quantum information with Rydberg atoms. *Rev. Mod. Phys.* **82,** 2313–2363 (2010) (cit. on pp. 1, 4).

27. Schauß, P. *et al.* Crystallization in Ising quantum magnets. *Science* **347,** 1455–1458 (2015) (cit. on pp. 1, 6, 8, 10).

28. Levine, H. *et al.* High-Fidelity Control and Entanglement of Rydberg-Atom Qubits. *Phys. Rev. Lett.* **121,** 123603 (2018) (cit. on pp. 1, 9, 10, 12).

29. Hollerith, S. *et al.* private communication. manuscript in preparation. (Cit. on p. 1).

30. Zeiher, J. *et al.* Many-body interferometry of a Rydberg-dressed spin lattice. *Nature Physics* **12,** 1095 (2016) (cit. on p. 1).

31. Kaufman, A. M., Lester, B. J. & Regal, C. A. Cooling a Single Atom in an Optical Tweezer to Its Quantum Ground State. *Phys. Rev. X* **2,** 041014 (2012) (cit. on p. 1).

32. Barredo, D., Lienhard, V., de Léséleuc, S., Lahaye, T. & Browaeys, A. Synthetic three-dimensional atomic structures assembled atom by atom. *Nature* **561,** 79–82 (2018) (cit. on p. 1).

33. Lester, B. J., Luick, N., Kaufman, A. M., Reynolds, C. M. & Regal, C. A. Rapid Production of Uniformly Filled Arrays of Neutral Atoms. *Phys. Rev. Lett.* **115,** 073003 (2015) (cit. on p. 1).

34. Bernien, H. *et al.* Probing many-body dynamics on a 51-atom quantum simulator. *Nature* **551,** 579 (2017) (cit. on p. 1).
35. Saßmannshausen, H., Merkt, F. & Deiglmayr, J. High-resolution spectroscopy of Rydberg states in an ultracold cesium gas. *Phys. Rev. A* **87,** 032519 (2013) (cit. on p. 3).
36. Gallagher, T. F. *Rydberg Atoms* (Cambridge University Press, 1994) (cit. on p. 3).
37. Seaton, M. J. Quantum defect theory. *Reports on Progress in Physics* **46,** 167–257 (1983) (cit. on p. 4).
38. Beterov, I. I., Ryabtsev, I. I., Tretyakov, D. B. & Entin, V. M. Quasiclassical calculations of blackbody-radiation-induced depopulation rates and effective lifetimes of Rydberg nS, nP, and nD alkali-metal atoms with $n \leq 80$. *Phys. Rev. A* **79,** 052504 (2009) (cit. on p. 5).
39. Šibalic, N., Pritchard, J. D., Adams, C. S. & Weatherill, K. J. ARC: An open-source library for calculating properties of alkali Rydberg atoms. *Computer Physics Communications* **220,** 319–331 (2017) (cit. on p. 5).
40. Scully, M. & Zubairy, M. *Quantum Optics* (Cambridge University Press, 1997) (cit. on pp. 5, 6).
41. De Léséleuc, S., Barredo, D., Lienhard, V., Browaeys, A. & Lahaye, T. Analysis of imperfections in the coherent optical excitation of single atoms to Rydberg states. *Phys. Rev. A* **97,** 053803 (2018) (cit. on pp. 5, 8, 10, 12, 13).
42. Isenhower, L., Saffman, M. & Mølmer, K. Multibit CkNOT quantum gates via Rydberg blockade. *Quantum Information Processing* **10,** 755 (2011) (cit. on p. 6).
43. Zeiher, J. *Realization of Rydberg-dressed quantum magnets* PhD thesis (Ludwig-Maximilians-Universität München, 2017) (cit. on pp. 7, 19, 20, 24).
44. Henkel, N. *Rydberg-dressed Bose-Einstein condensates* PhD thesis (Technische Universität Dresden, 2013) (cit. on p. 7).
45. Tiecke, T. G. Properties of Potassium (2011) (cit. on p. 8).
46. Walter, A.-S. *Design and Characterization of an UV Lasersystem for Rydberg Experiments with Potassium* master thesis. forthcoming (cit. on p. 8).
47. McKay, D. Potassium 5p Line Data (2009) (cit. on pp. 9, 10).
48. Picken, C. J., Legaie, R., McDonnell, K. & Pritchard, J. D. Entanglement of neutral-atom qubits with long ground-Rydberg coherence times. arXiv: 1808.04755 (2018) (cit. on p. 8).
49. Xu, W. & DeMarco, B. Velocity-selective electromagnetically-induced-transparency measurements of potassium Rydberg states. *Phys. Rev. A* **93,** 011801 (2016) (cit. on p. 9).
50. Bromage, J. Raman Amplification for Fiber Communications Systems. *J. Lightwave Technol.* 79 (2004) (cit. on p. 10).
51. Risk, W. P., Gosnell, T. R. & Nurmikko, A. V. *Compact Blue-Green Lasers* (Cambridge University Press, 2003) (cit. on p. 16).

52. Boyd, R. *Nonlinear Optics* (Elsevier Science, 2008) (cit. on pp. 16, 17).

53. Riedel, R. *et al.* Thermal properties of borate crystals for high power optical parametric chirped-pulse amplification. *Opt. Express* **22,** 17607–17619 (2014) (cit. on p. 17).

54. Armstrong, D. J., Alford, W. J., Raymond, T. D. & Smith, A. V. Absolute measurement of the effective nonlinearities of KTP and BBO crystals by optical parametric amplification. *Appl. Opt.* 2032–2040 (1996) (cit. on p. 17).

55. Nikogosyan, D. N. Beta barium borate (BBO). *Applied Physics A* **52,** 359–368 (1991) (cit. on p. 17).

56. SNLO nonlinear optics code available from A. V. Smith, AS-Photonics, Albuquerque, NM (cit. on p. 17).

57. Boyd, G. D. & Kleinman, D. A. Parametric Interaction of Focused Gaussian Light Beams. *Journal of Applied Physics* **39,** 3597–3639 (1968) (cit. on p. 18).

58. Chen, Y. & Chen, Y. Analytical functions for the optimization of second-harmonic generation and parametric generation by focused Gaussian beams. *Applied Physics B* **76,** 645–647 (2003) (cit. on p. 18).

59. Burkley, Z., Rasor, C., Cooper, S. F., Brandt, A. D. & Yost, D. C. Yb fiber amplifier at 972.5 nm with frequency quadrupling to 243.1 nm. *Applied Physics B* **123,** 5 (2016) (cit. on p. 20).

60. Meyer, H.-M. *A Laser-System for Trapping and Cooling of Ytterbium-Ions* diploma thesis. 2010 (cit. on pp. 20, 23).

61. Brozek, O. S. *Effiziente Frequenzverdopplung mit Diodenlasern* diploma thesis. 1995 (cit. on p. 20).

62. Langer, P. *Aufbau einer Lasersystems bei 297 nm zur Einphotonenanregung von Rydbergzuständen in Rubidium* diploma thesis. 2012 (cit. on pp. 20, 23, 52).

63. Werner, J. *Kontinuierliches Laden einer Magnetfalle mit lasergekühlten Chromatomen* master thesis. 2000 (cit. on p. 21).

64. Kogelnik, H. & Li, T. Laser Beams and Resonators. *Appl. Opt.* **5,** 1550–1567 (1966) (cit. on p. 21).

65. Hanna, D. Astigmatic Gaussian beams produced by axially asymmetric laser cavities. *IEEE Journal of Quantum Electronics* **5,** 483–488 (1969) (cit. on p. 21).

66. Jenkins, F. & White, H. *Fundamentals of Optics* (Tata McGraw-Hill Education, 1937) (cit. on p. 22).

67. Ashkin, A., Boyd, G. & Dziedzic, J. Resonant optical second harmonic generation and mixing. *IEEE Journal of Quantum Electronics* **2,** 109–124 (1966) (cit. on p. 24).

68. Polzik, E. S. & Kimble, H. J. Frequency doubling with KNbO3 in an external cavity. *Opt. Lett.* **16,** 1400–1402 (1991) (cit. on p. 24).

69. Ricci, L. *et al.* A compact grating-stabilized diode laser system for atomic physics. *Optics Communications* **117,** 541–549 (1995) (cit. on p. 29).

70. Cook, E. C., Martin, P. J., Brown-Heft, T. L., Garman, J. C. & Steck, D. A. High passive-stability diode-laser design for use in atomic-physics experiments. *Review of Scientific Instruments* **83,** 043101 (2012) (cit. on p. 30).

71. Janša, N. *A frequency-stable diode laser system for spectroscopy and trapping of Sr atoms* master thesis. 2016 (cit. on pp. 31, 37).

72. *TAPERED AMPLIFIER GaAs Semiconductor Laser Diode* EYP-TPA-0808-02000-4006-CMT04-0000. Datasheet. Eagleyard (2018) (cit. on p. 33).

73. Duda, M. *A Laser System for Cooling and Trapping Potassium-39* master thesis. 2017 (cit. on p. 34).

74. Flaucher, I. *Implementation and Characterization of a Laser Set-up for Raman Cooling* bachelor thesis. 2018 (cit. on pp. 35, 61).

75. Alnis, J., Matveev, A., Kolachevsky, N., Udem, T. & Hänsch, T. W. Subhertz linewidth diode lasers by stabilization to vibrationally and thermally compensated ultralow-expansion glass Fabry-Pérot cavities. *Phys. Rev. A* **77,** 053809 (2008) (cit. on p. 38).

76. Osterholz, P. *Stabilisation of a Diode Laser to a High Finesse ULE Cavity* bachelor thesis. 2017 (cit. on p. 38).

77. Lally, E. M. *A Narrow-Linewidth Laser at 1550 nm Using the Pound-Drever-Hall Stabilization Technique* master thesis. 2006 (cit. on p. 38).

78. Poirson, J., Bretenaker, F., Vallet, M. & Floch, A. L. Analytical and experimental study of ringing effects in a Fabry–Perot cavity. Application to the measurement of high finesses. *J. Opt. Soc. Am. B* **14,** 2811–2817 (1997) (cit. on p. 40).

79. Martin, M. J. *Quantum Metrology and Many-Body Physics: Pushing the Frontier of the Optical Lattice Clock* PhD thesis (University of Colorado, 2013) (cit. on p. 41).

80. Drever, R. W. P. *et al.* Laser phase and frequency stabilization using an optical resonator. *Applied Physics B* **31,** 97–105 (1983) (cit. on p. 43).

81. Black, E. D. An introduction to Pound-Drever-Hall laser frequency stabilization. *American Journal of Physics* **69,** 79–87 (2001) (cit. on p. 43).

82. Gustafsson, U., Alnis, J. & Svanberg, S. Atomic spectroscopy with violet laser diodes. *American Journal of Physics* **68,** 660–664 (2000) (cit. on p. 47).

83. Briles, T. C., Yost, D. C., Cingöz, A., Ye, J. & Schibli, T. R. Simple piezoelectric-actuated mirror with 180 kHz servo bandwidth. *Opt. Express* **18,** 9739–9746 (2010) (cit. on p. 52).

84. Baillard, X. *et al.* Interference-filter-stabilized external-cavity diode lasers. *Optics Communications* **266,** 609 –613 (2006) (cit. on pp. 61, 71).

85. Shirley, J. H. Modulation transfer processes in optical heterodyne saturation spectroscopy. *Opt. Lett.* **7,** 537–539 (1982) (cit. on p. 61).

List of Figures

List of Tables

Acknowledgements

In the course of this thesis I had a great time, made good friends and learned so many things, ranging from different kinds of screws and using Python to the fascinating world of cold atoms. For this I want to thank

- Immanuel Bloch for taking formal supervision of this thesis, for offering me a PhD position in his Fermi gas microscope and most of all for making me turn to experimental physics by his intriguing lectures.
- Christan Groß for supervising my project, for always bringing a good mood to the lab, for finding a solution to every problem and for his way of working which I admire a lot.
- Lorenzo Festa for helping me with my project and taking a lot of the organizational and background work from me. It was a great time working with him.
- Nikolaus Lorenz and Marcel Duda for sharing their knowledge and helping me with my technical problems no matter how annoying I was.
- Anne-Sophie Walter for being the best officemate anyone could wish for and for allowing me to build on her great work for the doubling cavities. Without her, my project, especially the doubling cavity, would not have been possible.
- Johannes Zeiher for always taking time to answer my questions and sharing his vast knowledge, for being motivating, and a great physicist to look up to.
- For proofreading and giving very helpful advice for my thesis, figures and plots I would like to thank Christian Gross, Lorenzo Festa, Marcel Duda, Philip Osterholz and Antonio Rubio Abadal.
- And the whole Bloch group for a wonderful year. I enjoyed the time with all of you so much, that I am gonna stay here.

Finally and most importantly I want to thank my parents, who supported me during my studies and all my life.

Erklärung

Hiermit erkläre ich, die vorliegende Arbeit selbständig verfasst zu haben und keine anderen als die in der Arbeit angegebenen Quellen und Hilfsmittel benutzt zu haben.

Ort, Datum	Unterschrift